Pre-industrial, present and future atmospheric soluble iron deposition and the role of aerosol acidity and oxalate under CMIP6 emissions

Elisa Bergas-Massó[1,2], María Gonçalves Ageitos[1,2], Stelios Myriokefalitakis[3], Ron L. Miller[4], Twan van Noije[5], Philippe Le Sager[5], Gilbert Montané Pinto[1], Carlos Pérez García-Pando[1,6]

[1]Barcelona Supercomputing Center (BSC), Barcelona, Spain
[2]Universitat Politècnica de Catalunya (UPC), Barcelona, Spain
[3]Institute for Environmental Research and Sustainable Development (IERSD), National Observatory of Athens, Penteli, Greece
[4]NASA Goddard Institute for Space Studies, New York, NY, US
[5]Royal Netherlands Meteorological Institute (KNMI), De Bilt, The Netherlands
[6]ICREA, Catalan Institution for Research and Advances Studies, Barcelona, Spain

Key Points:

- Global soluble iron deposition will increase (decrease) by 40% (35%) with weak (strong) climate mitigation policies
- Aerosol acidity controls the dissolution of iron from dust sources and oxalate from combustion sources in past, present and future scenarios
- Future soluble iron deposition decreases (increases) over the Southern Ocean (the equatorial Pacific) regardless of the mitigation policy

Corresponding author: Elisa Bergas-Massó, elisa.bergas@bsc.es

Abstract

Changes in atmospheric iron (Fe) deposition to the open ocean affect net primary productivity, nitrogen fixation, and carbon uptake rates. We investigate the changes in soluble Fe (SFe) deposition from the pre-industrial period to the late 21st century using the EC-Earth3-Iron Earth System model, which stands out for its comprehensive representation of the atmospheric oxalate, sulfate, and Fe cycles. We show how anthropogenic activity has modified the magnitude and spatial distribution of SFe deposition by increasing combustion Fe emissions along with atmospheric acidity and oxalate levels. We find that SFe deposition has doubled since the early Industrial Era using the Coupled Model Intercomparison Project Phase 6 (CMIP6) emission inventory, with acidity being the main solubilization pathway for dust Fe, and ligand-promoted (oxalate) processing dominating the solubilization of combustion Fe. We project a global SFe deposition increase of 40% by the late 21st century relative to present day under Shared Socioeconomic Pathway (SSP) 3-7.0, which assumes weak climate change mitigation policies. In contrast, sustainable and business-as-usual SSPs (1-2.6 and 2-4.5) result in 35% and 10% global decreases, respectively. Despite these differences, SFe deposition consistently increases and decreases across SSPs over the (high nutrient low chlorophyl) equatorial Pacific and Southern Ocean (SO), respectively. Future changes in dust and wildfires with climate remains a key challenge for constraining SFe projections. Results show that the equatorial Pacific and the SO would be sensitive not only to changes in Australian or South American dust emissions, but also to those in North Africa.

Plain Language Summary

Marine biota needs bioavailable (or soluble) iron (Fe) as a nutrient for photosynthesis. Given that photosynthesis captures atmospheric carbon dioxide (CO_2), the amount and spatial distribution of soluble Fe (SFe) deposited regulate the capacity of the ocean to store CO_2 and hence can affect the global climate. The supply of Fe to the atmosphere is dominated by desert dust aerosols created by wind erosion of arid surfaces, with a minor contribution from combustion processes aerosols. Freshly emitted dust-Fe is mainly insoluble but is partly transformed into SFe species during atmospheric transport through various dissolution mechanisms mainly affected by aerosol acidity and oxalate concentrations. We conduct a modeling study to quantitatively understand how changes in aerosol and gas-phase species emissions from the early industrial era to the late 21st century alter SFe deposition. Our simulations indicate that SFe deposition has doubled since the beginning of the Industrial Era. Future estimates depend upon the projected socio-economic scenario, with solubilization being boosted in the scenario with weaker mitigation poli-

cies, and vice versa. Results show that understanding changes in aerosol acidity and oxalate concentrations, along with changes in dust and wildfires with climate are key to constrain projections of SFe deposition.

1 Introduction

Since the Industrial Revolution, the release of gases and aerosols into the atmosphere due to human activities has strongly increased. Consequently, atmospheric concentrations of greenhouse gases, in particular carbon dioxide (CO_2), are now far higher than in any period over the past several hundred-thousand years (EPICA, 2004). About a quarter of the CO_2 emitted to the atmosphere since the Industrial Revolution has been absorbed and stored by the ocean (Ciais et al., 2013). The ability of the ocean to capture CO_2 depends partly on ocean net primary productivity (NPP), i.e., the rate of photosynthetic carbon fixation minus the fraction of fixed carbon used for respiration and maintenance by marine biota. Ocean NPP relies upon the availability of light and nutrients, e.g., nitrogen, phosphorus, iron (Fe), and silica (Behrenfeld et al., 2007). A vast area of oceanic surface waters is depleted in Fe but not in other nutrients, e.g., the Southern Ocean (SO), the eastern equatorial Pacific, and the subarctic Pacific (Boyd et al., 2005). In those regions, so-called high nutrient low chlorophyll (HNLC) regions, Fe is the limiting factor for phytoplankton productivity, and thus for NPP (Jickells et al., 2005). Therefore, the availability of Fe may significantly affect the ocean biological carbon export on a global scale. This correlation between Fe supply to the ocean and the ocean CO_2 uptake, opened a scientific debate on the potential use of Fe to fertilize the global ocean in order to increase the uptake of CO_2 from the atmosphere, the so-called "Iron Hypothesis" (Martin & Fitzwater, 1988; Martin, 1990; Stoll, 2020).

Fe reaches the oceans mainly from estuary runoff and suspended sediment from continental margins. However, these fluvial and glacial particulate Fe inputs are restricted to near-coastal areas and the dominant Fe input to the open ocean is atmospheric aerosol deposition (Duce & Tindale, 1991). The major contributor to atmospheric Fe is mineral dust emitted from arid and semiarid regions, with an estimated present-day contribution of 95% of the total Fe aerosol burden. The remaining 5% is attributed to combustion sources, particularly anthropogenic combustion and biomass burning aerosols (Luo et al., 2008). However, not all Fe deposited to the ocean is directly bioavailable for marine biota. Much uncertainty exists about the physicochemical Fe forms that can be processed as nutrients (Lis et al., 2015; Baker & Croot, 2010; Jickells et al., 2005). It is widely assumed that soluble Fe (SFe) forms (e.g., aqueous, colloidal, or nanoparticulate) can be considered as bioavailable (Baker et al., 2006). Fe in dust (FeD) is considered to be

largely insoluble at emission (≈0.1%) (Mahowald et al., 2005; K. S. Johnson, 2001; Jickells & Spokes, 2001; Sholkovitz et al., 2012; Schroth et al., 2009). On the other hand, the solubility of combustion Fe (FeC), both from fossil fuels (FeF) and biomass burning (FeB) emissions, is known to be higher and is estimated to range from 8 to 81% depending on the fuel type or activity sector (Chuang et al., 2005; Schroth et al., 2009; Rathod et al., 2020).

Observational and experimental evidence point towards an increase in Fe solubility downwind of the sources (Rizzolo et al., 2017; Zhuang et al., 1992a; Rodríguez et al., 2021). Acidic processing has been identified as a crucial Fe solubilization mechanism in the atmosphere, occurring at low pH either in cloud droplets or in aerosol water (Spokes et al., 1994; Desboeufs et al., 1999; Zhuang et al., 1992b; Nenes et al., 2011). In addition, oxalate (hereafter OXL), can act as an organic ligand promoting Fe solubilization by effectively breaking the Fe-O bonds at the surface of the aerosol via the formation of ligand-containing surface structures (Yoon et al., 2004; Li et al., 2018). Photoreductive processes are also considered to be a non-negligible pathway to Fe dissolution, although their contribution might be lower than for acidic and OXL-promoted dissolution (Key et al., 2008). Aerosol acidity, atmospheric OXL, and therefore SFe estimates are governed by multiphase processes. Such processes significantly impact the atmospheric cycles of inorganic species like sulfur (Hoyle et al., 2016; Steinfeld, 1998; Tsai et al., 2010) and hence sulfate (SO_4^{2-}), which is known to be the main control on aerosol liquid water content and aerosol acidity. Multiphase chemistry also acts as a complementary pathway for the formation of organic species related to Fe dissolution, such as OXL. SO_4^{2-} and OXL are, in fact, the most common species formed via aqueous-phase reactions of inorganic and organic origin, respectively (e.g., Lim et al., 2010; Carlton et al., 2007). SO_4^{2-} is mainly produced via oxidation of dissolved sulfur dioxide (SO_2) (Steinfeld, 1998) and OXL is primarily formed through cloud processing of glyoxal and other water-soluble products of alkenes and aromatics of anthropogenic, biogenic, and marine origin (Carlton et al., 2007; Warneck, 2003).

Models along with observations can be used to better understand and constrain the atmospheric Fe supply to the oceans, but SFe concentrations and deposition measurements are scarce and heterogeneous (e.g., sediment traps, marine sediment cores, or direct deposition measurements from scientific cruises) (Schulz et al., 2012). Modelling is therefore key to analyze geographical regions not covered by observations and even make assessments at global scales, to understand the different sources and processes affecting SFe deposition, and to assess their impacts on the ocean and the climate. However, estimating the atmospheric supply of SFe to the global ocean with models is challenging

due to the variety and complexity of Fe forms in aerosols and the processes that alter their solubility. Over the last decade, models have seen advances in the representation of Fe emission sources and subsequent atmospheric processing. Early works neglected Fe sources such as combustion aerosols (Hand et al., 2004; M. S. Johnson & Meskhidze, 2013; Moxim et al., 2011), which have been later identified as relevant contributors to the atmospheric SFe (Guieu et al., 2005; Ito et al., 2021; Luo et al., 2008). Atmospheric dissolution has been represented with different levels of complexity in models. Simple approaches exist following first-order rate processing constants and considering a globally uniform 3.5% of Fe content in dust (e.g., Duce & Tindale, 1991; Luo et al., 2008; Hand et al., 2004). Mid-complexity representations allow for different types of acidic species to interact with dust, and consider mineral-specific dissolution rates (Meskhidze et al., 2005; Ito & Xu, 2014). Some models further account for OXL processing, even when the full complexity of the OXL formation in cloud water is not explicitly considered, but parameterized (Scanza et al., 2018; M. S. Johnson & Meskhidze, 2013; Hamilton et al., 2020). More recently, complex schemes have been developed where both FeD and FeC are dissolved during atmospheric transport, multiphase chemistry is resolved explicitly including the OXL and sulfur cycles, and aerosol acidity is considered in both accumulation and coarse aerosol modes that account for aerosol microphysics (Myriokefalitakis et al., 2015, 2021).

While the present-day Fe cycle has been estimated in numerous studies, changes in the atmospheric Fe cycle that have occurred over the industrial period or that are expected to occur over the 21st century have been less explored, and only with simple or intermediate-complexity schemes. Modelling studies focusing on the present day estimate a global atmospheric dissolved Fe deposition flux into the ocean in the range 0.1–0.8 Tg-Fe yr-1 (Hamilton et al., 2020, 2019; Ito et al., 2019; Myriokefalitakis et al., 2018; Scanza et al., 2018; Ito & Shi, 2016; Luo et al., 2008) (Table S1). Some studies estimate that pre-industrial Fe would have been at least 2 times lower, mainly due to lower emission of sulfate and nitrate precursors leading to a decline in proton-promoted solublization (e.g., Myriokefalitakis et al., 2015); other studies, however, point towards higher values (Hamilton et al., 2020) due to a possible underestimation of wildfires in the pre-industrial era in commonly used emission datasets such as the Coupled Model Intercomparison Project Phase 6 (CMIP6) inventory (Hamilton et al., 2018). Despite the large uncertainties, it has been accepted that the rise in anthropogenic combustion emissions since pre-industrial times has increased the Fe atmospheric burden along with atmospheric acidity due to a drastic increase in SO_2 emissions (Smith et al., 2004; Hand et al., 2012). Future projections are even more uncertain as anthropogenic and fire emissions depend on hypothetical future human activities and the impact of land-use change and climate change

on dust emission sources and fires is complex to estimate (Mahowald et al., 2009; Harris et al., 2016).

In this work, we aim to estimate the pre-industrial, present and future atmospheric delivery of SFe to the ocean by using the state-of-the-art Earth System Model (ESM) EC-Earth3-Iron (Myriokefalitakis et al., 2021). The atmospheric Fe cycle component in EC-Earth3-Iron contains numerous advances including a detailed atmospheric Fe solubilization mechanism that accounts for complex multiphase chemistry driving aerosol acidity and explicit representation of OXL. With our novel model capabilities, we estimate the SFe deposition into the ocean, and assess aerosol acidity, OXL and their effects upon Fe solubilization, while quantifying the contribution of natural and anthropogenic sources for pre-industrial and present-day conditions, and a range of future scenarios, following the Shared Socioeconomic Pathways (SSPs) of the CMIP6 (Eyring et al., 2016). While our main focus is SFe and its drivers, our assessment of aerosol acidity and OXL in future scenarios has been barely tackled, if at all, in previous literature, and their implications go well beyond the Fe cycle.

The manuscript is organized as follows: We first describe the model and the experimental setup (Section 2). We then present and discuss the Fe emissions in each scenario and the corresponding simulated global aerosol acidity, OXL surface concentrations and the resulting SFe atmospheric deposition budgets and their distributions and source contribution for pre-industrial, present and future scenarios (Section 3). Finally, we summarize the relevant findings and discuss their implications, along with the plans for future research (Section 4).

2 Methods

2.1 Model Description

EC-Earth3 is an ESM comprised of modules, each of them representing a different Earth System component, i.e., the atmosphere, ocean, sea ice, land surface, dynamic vegetation, atmospheric composition, and ocean biogeochemistry, which can be coupled in various model configurations according to different scientific needs (see Döscher et al., 2021, for details). In this study we apply the recently developed EC-Earth3-Iron model configuration (Myriokefalitakis et al., 2021), which is an extended version of the CMIP6 EC-Earth3-AerChem configuration (Van Noije et al., 2021). We perform all simulations in atmosphere-only mode, in which the atmospheric general circulation model: the Integrated Forecasting System (IFS) from the European Centre for Medium-Range Weather Forecasts (ECMWF), is coupled to the atmospheric chemistry module: the Tracer Model

version 5 release 3.0 (TM5-MP 3.0). With this setup, sea-surface temperatures (SSTs) and sea-ice concentrations (SICs) are prescribed as in the Atmospheric Model Intercomparison Project (AMIP) experiment (Gates et al., 1999; Döscher et al., 2021). In EC-Earth3-Iron, the atmospheric model can also be coupled to the ocean (Nucleus for European Modelling of the Ocean (NEMO version 3.6, Rousset et al. (2015))) and sea-ice (LIM3, Vancoppenolle et al. (2009)) components. For our analyses, that focus on the atmospheric cycle of Fe, the atmosphere-only mode is thought to constitute a valid and computationally efficient approach.

TM5-MP 3.0 represents interactive aerosols and tropospheric chemistry. In our setup, the gas-phase chemistry scheme is resolved by the MOGUNTIA chemical mechanism (Myriokefalitakis, Daskalakis, et al., 2020). SO_4^{2-}, black carbon (BC), organic aerosols (OA), sea salt, and mineral dust microphysics are described by the modal aerosol scheme M7 (Vignati et al., 2004). M7 defines seven log-normal modes to represent the aerosols' size distribution and mixing state; four water-soluble modes (nucleation, Aitken, accumulation, and coarse) and three insoluble modes (Aitken, accumulation, and coarse). Natural emissions of mineral dust, sea salt, marine dimethyl sulfide (DMS), and nitrogen oxides from lighting are calculated online, while other natural emissions are prescribed (e.g. biogenic emissions of non-methane volatile organic compounds). Mineral dust emission is parameterized according to Tegen et al. (2002).

EC-Earth3-Iron includes a representation of the atmospheric Fe cycle, and explicitly calculates the dissolution of Fe in aerosol water and in cloud droplets, aqueous-phase OXL formation, and cloud and aerosol acidity, the latter in both accumulation and coarse modes. Its ability to represent tropospheric aerosols has been shown elsewhere (Myriokefalitakis et al., 2021), and remains similar to the standard EC-Earth3-AerChem version (Gliß et al., 2021), regardless of the substantial differences in the gas-phase and aqueous chemistry. For details and extended comparisons with observations of EC-Earth3-Iron we refer to Myriokefalitakis et al. (2021). Below we provide a summary of the main features related to the calculation of SFe.

2.1.1 Atmospheric Fe cycle, aerosol acidity and oxalate in EC-Earth3-Iron

EC-Earth3-Iron calculates the dissolution of Fe in aerosol water and in cloud droplets. Four different Fe pools are considered (Shi et al., 2011) according to their susceptibility to dissolve: 1) A fast dissolution pool that relates to ferrihydrite (i.e., hydrated ferric Fe oxide) on the surface of minerals; 2) an intermediate dissolution pool that considers nano-sized Fe oxides from the surface of dust minerals; 3) a slow dissolution pool

that takes into account the Fe release from heterogeneous inclusion of nano-Fe grains in the internal mixture of various dust minerals, such as aluminosilicates, hematite, and goethite; and 4) a separate Fe pool for combustion aerosols (Ito, 2015; Myriokefalitakis et al., 2021).

This version of the model explicitly traces the three Fe pools and calcium (Ca) originated from mineral dust sources. The emitted dust Fe (FeD) in the accumulation and coarse insoluble modes of each pool are based on the soil mineralogy of Claquin et al. (1999), including the updates proposed in Nickovic et al. (2012). The Fe content of each mineral is based on Nickovic et al. (2013). Brittle Fragmentation Theory (Kok, 2011; Pérez García-Pando et al., 2016; Perlwitz et al., 2015a, 2015b) is used to have a better estimation of particle size distribution of each mineral at emission. Following Ito and Shi (2016), we assume an initial solubility (i.e., the fraction of soluble FeD, SFeD, over total FeD) of 0.1% for all Fe mineral soil emissions. For more details on FeD emissions in the model, we refer to Myriokefalitakis et al. (2021).

FeC emissions, including FeF and FeB emissions, are derived following Ito et al. (2018) and Hajima et al. (2019). FeC emissions are computed by applying specific emission factors to the total particulate emissions (i.e., the sum of organic carbon and black carbon emissions) for each aerosol mode considered and activity sector (i.e., energy, industrial, iron and steel industries, residential and commercial, shipping, waste treatment and biomass burning). FeC emissions are assumed here to be insoluble, except for ship oil combustion ($\approx 80\%$ solubility). The FeF emission factors have inter-annual variability with year-to-year changes only due to changes in the OC and BC emissions (Ito et al., 2018) during the historical period, but are assumed to be constant in the future (set to the latest available value of the historical period). For FeB, the emission factors are kept constant following Ito et al. (2018). For more details on FeC emissions in the model, we refer to Myriokefalitakis et al. (2021).

The dissolution of Fe from mineral dust and Fe from combustion processes in each of the pools depends on the acidity levels of the solution (i.e., proton-promoted Fe dissolution), the OXL concentration (i.e., ligand-promoted Fe dissolution), and irradiation (photo-reductive Fe dissolution), following Ito (2015) and Ito and Shi (2016). Estimates of the degree of acidity of particles and clouds affecting proton-promoted Fe solubilization rely on the use of the thermodynamic model ISORROPIA II (Fountoukis & Nenes, 2007). ISORROPIA II is used to predict not only acidity but also equilibrium gas-particle partitioning, liquid-phase activity coefficients, solid-liquid and liquid-liquid equilibria, dynamic mass transfer of semivolatile species and aerosol liquid water content. The modeling approach in ISORROPIA II does not consider single-ion activity coefficients that allow the calculation of pH as proxy of acidity, but instead the pH values presented in

this work are based on the free-H^+ molality. More details on the multiphase chemistry included in the model can be found in Myriokefalitakis et al. (2021). OXL concentrations have a non-negligible influence on Fe solubilization, hence the formation of OXL is computed online in the model taking into consideration aqueous phase chemistry (Myriokefalitakis et al., 2021). OXL is rapidly formed via biomass combustion processes in the atmosphere (Kundu et al., 2010). Even if the direct emission of OXL is very low compared to secondary formation, EC-Earth3-Iron includes OXL primary emissions obtained as a fraction of biomass burning and anthropogenic wood burning BC emissions, 0.763% (Yamasoe et al., 2000), and 0.863% (Schmidl et al., 2008), respectively.

2.2 Experimental Setup

In order to consistently quantify OXL concentrations, aerosol acidity and SFe deposition for pre-industrial, present and future climates, we perform five ensembles of atmosphere-only time-slice experiments. Each ensemble is composed of 30 different members where the atmospheric initial conditions have been created by applying infinitesimal random perturbations, with the aim of sampling the internal climate variability. The initial conditions for the atmospheric tracers, gas-phase and aerosols, use 2 years of spin-up to ensure realistic concentrations at the global scale, the third year of simulation is used to construct the ensembles presented in this work. Those were run with IFS and TM5-MP coupled, where potential feedbacks between the atmosphere and the ocean are neglected. Also, to maintain consistent conditions between the atmosphere and the ocean state, the aerosols and gas-phase species were not allowed to interact with the atmospheric state. The IFS horizontal resolution is T255 (i.e., a spacing of roughly 80 km), 91 layers are used in the vertical direction up to 0.01 hPa, and a time step of 45 min is applied. On the other hand, TM5-MP has an horizontal resolution of 3° in longitude by 2° in latitude and uses 34 layers to represent the vertical direction up to 0.1 hPa (≈60 km).

We simulated time-slices that represent pre-industrial (PI) and present-day (PD) conditions along with three different future scenarios based on Tier-1 CMIP6 Shared Socioeconomic Pathways (SSPs) (O'Neill et al., 2016) (SSP1-2.6, SSP2-4.5 and SSP3-7.0) that respectively represent forcing levels of 2.6, 4.5 and 7.0 W/m^2 by the end of this century. The PD simulation considers climatological conditions based on CMIP6 historical for the 1985-2014 period and serves as a baseline for the assessment of past and future changes. To reproduce the PI climatological conditions, CMIP6 historical information for the 1850-1879 period is used. For the future scenarios, the climatological period considered is 2070-2099 (Table 1).

Among the three future scenarios, SSP1-2.6 represents a more optimistic and sustainable pathway that lies in the lower end of SSP ranges in terms of future forcing pathways and emissions of Near-Term Climate Forcers (NTCF). In this scenario, demand of energy- and resource-intensive agricultural commodities such as ruminant meat is significantly lower than for present-day demand, and pollution controls are expanded, especially in high-income economies. The SSP2-4.5 is a business-as-usual scenario that falls in the medium part of the range of future forcing pathways and NTCF emissions. This socioeconomic pathway projects a moderate population growth, and an increase in food consumption and a continued growth of greenhouse gases (GHGs) emissions while some efforts are made to eventually decrease pollutant emissions. The SSP3-7.0 is in the middle to higher end of the SSP range in terms of future forcing pathways, with high NTCF emissions (particularly SO_2) and substantial land-use change (in particular decreased global forest cover). Within this scenario, population is expected to increase in low- and middle-income countries, a resurgence of coal dependence is seen and policymaking to control air pollution and GHGs emissions is ineffective.

Climatological monthly emission fields for the selected present-day and future 30-yr periods for both anthropogenic and natural species (not computed online) are generated specifically for each of the experiments from Earth System Grid Federation (ESGF) archives (https://esgf-node.llnl.gov/search/cmip6). For the pre-industrial period, fixed 1850 emissions are used. The historical anthropogenic emissions used for our PI and PD simulations are taken from the Community Emissions Data System (Hoesly et al., 2018) and the historical fire emissions from the BB4CMIP6 data set (van Marle et al., 2017). Future emission data for each scenario are detailed in Gidden et al. (2019).

The experiments use prescribed sea surface temperature (SST) and sea ice concentration (SIC) climatologies created from a selection of historical and scenario simulations performed with the coupled atmosphere-ocean version of EC-Earth3, all contributing to the CMIP6 exercise. For each of the selected periods (1850-1879 for the pre-industrial, 1985-2014 for the present, and 2070-2099 for the future scenarios), seven realizations available in the ESGF repository were used to account for potential differences due to the sampling of internal climate variability. The corresponding climatological ocean and sea ice boundary conditions for each experiment were produced by first averaging across the seven realizations and then, averaging in time each 30-year period, ending up with a climatological average for each calendar month.

Global estimates of dust emission largely vary across state-of-the-art ESMs (Wu et al., 2020; Gliß et al., 2021) ranging from 735 to 8186 Tg yr^{-1}. Differences arise due to diverse representation of dust emission in models with different dependence on envi-

Table 1. List of simulations done in this work with its time period, prescribed emissions, and regions where dust has been perturbed.

Experiment	Time period	Prescribed emissions	Dust-region pert.*
PI	1850	CMIP6 historical	-
PD	1985-2014	CMIP6 historical	-
SSP126	2070-2099	CMIP6 SSP1-2.6	-
SSP245	2070-2099	CMIP6 SSP2-4.5	-
SSP370	2070-2099	CMIP6 SSP3-7.0	-
SSP370-NAfr	2070-2099	CMIP6 SSP3-7.0	North Africa
SSP370-MEast	2070-2099	CMIP6 SSP3-7.0	Middle East
SSP370-EAsia	2070-2099	CMIP6 SSP3-7.0	East Asia
SSP370-SH	2070-2099	CMIP6 SSP3-7.0	Southern Hemisphere
SSP370-NAm	2070-2099	CMIP6 SSP3-7.0	North America

* The regions perturbed in each experiment are defined according to the Hemispheric Transport of Air Pollution (HTAP) project (Koffi et al., 2016) and can be seen in Figure S1a

ronmental and ambient factors (i.e., wind soil humidity, vegetation) or differences in the size distribution representation. Global and regional dust (and FeD) projections are even more uncertain (e.g., Ginoux et al., 2012; Kok et al., 2014; Mahowald, 2007) due to lack of confidence in future regional winds, precipitation, vegetation, and anthropogenic land-use change (Ginoux et al., 2012). In addition, Mahowald et al. (2002) and Yoshioka et al. (2007) show that the increase in dust surface concentrations observed between the 1960s and 1980s in Barbados is not captured by models and suggest that a change in dust source areas, to account for the creation of new deserts or human land use change, is required to match observations. In fact, most ESMs neglect the potential year-to-year evolution of relevant drivers of dust emission (e.g., changes in dust source area extent due to changes in vegetation and/or land-use). In particular, the EC-Earth3-Iron dust emission scheme relies on a vegetation field that considers exclusively intra-annual changes (Tegen et al., 2002). Therefore, dust projections with EC-Earth3-Iron depend upon changes in simulated wind and soil humidity. To account for these uncertainties and eventual changes in source area extent in the future, we perform an additional set of sensitivity experiments where dust emissions from different regions are perturbed.

Some studies suggest an increase of dust loading in response to future warming (Kok et al., 2018), while others project a decrease in dust emissions in key semi-arid regions

due to an increase in rainfall and vegetation (Pausata et al., 2020). Here, we explore the sensitivity of future SFe deposition to potential increases in dust emission. We define five simulations based on the the SSP370 scenario for the period 2070-2099. In each simulation we double the dust emission flux from a different source region: North Africa (NAfr), Middle East (MEast), East Asia (EAsia), Southern Hemisphere (SH) and North America (NAm). The regions selected are based on Koffi et al. (2016) and are shown in Figure S1a. Using SSP370 as our baseline allows understanding the sensitivity of regional and global SFe deposition to potential regional increases in dust emission when combustion emissions, aerosol acidity and OXL concentrations are the highest among scenarios, and thus likely not limiting factors of Fe solubilization.

To better understand the driving factors that result in changes in SFe deposition, we diagnose from our experiments the aerosols pH as a diagnostic of aerosol acidity. Yearly budget calculations are performed for variables such as Fe emission, solubilization, and deposition or OXL surface concentrations. The spread of the ensemble of those budgets (e.g., the difference between members of a simulation) is shown through the standard deviation (σ) with respect to the ensemble mean. Differences in fields of extensive variables (e.g., SFe deposition) are shown as relative differences in %, taking the PD scenario as reference. The statistical t-test with a 95% confidence interval is carried out over those relative difference fields to only show relative changes that are statistically significant (see Text S1).

3 Results and Discussion

3.1 Iron emissions

Our present-day simulation (PD) estimates a mean annual Fe emission for the 1985-2014 period of 42 $\pm$ 5 Tg Fe/yr (Figure 1). In agreement with previous studies (Luo et al., 2008; Mahowald et al., 2009), emissions from dust sources represent a 94.6% of total Fe emissions, while anthropogenic combustion and biomass burning represent the remaining 4.2 and 1.2 %, respectively. The mean emission for each Fe source is 40 $\pm$ 5 Tg Fe/yr for FeD, 1.75 Tg Fe/yr for FeF, and 0.52 Tg Fe/yr for FeB (no uncertainty is shown for FeF and FeB emissions as the same emission climatology is used for the 30 simulated single years). These estimates are in good agreement with prior studies, where FeD emissions estimates range between 35 and 72 Tg Fe/yr, FeF between 0.7 and 7.2 Tg Fe/yr and FeB between 0.16 and 2.2 Tg Fe/yr (Rathod et al., 2020; Hamilton et al., 2020, 2019; Scanza et al., 2018; Myriokefalitakis et al., 2018; Ito & Shi, 2016; Myriokefalitakis et al., 2015; Wang et al., 2015; Luo et al., 2008) (Table S2).

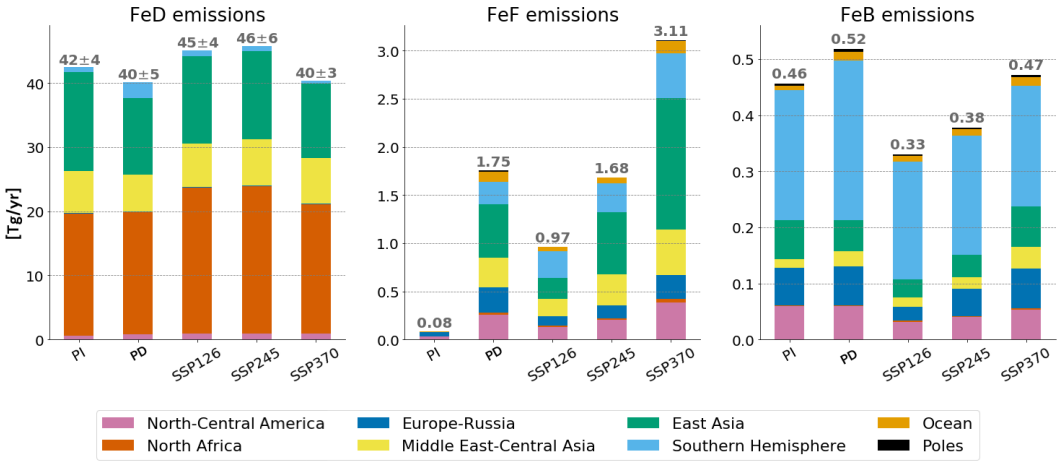

Figure 1. Mean annual emissions in Tg/yr of Fe from dust (FeD) (left panel), Fe from fossil fuels (FeF) (middle panel), Fe from biomass burning (FeB) (right figure) for each of the scenarios considered. The different colors represent the contribution of the different HTAP regions considered to the total emission budget.

FeD emissions contribute the most to the total Fe emission burden in all scenarios. Changes in FeD emissions between scenarios follow the changes in dust emissions. Mean annual dust emission budgets range between 860 and 970 Tg dust/yr for our pre-industrial, present, and future estimates with some variability among runs of the same ensemble ($\approx \pm$ 100 Tg Fe yr^{-1}) (Figure S2). These estimates fall in the lower limit of the simulated emission budget by other ESMs. This is partly due to current assumptions in the dust size distribution at emission and the lack of a super-coarse mode (Wu et al., 2020; Gliß et al., 2021). The variability in dust emissions is primarily controlled in our simulations by wind strength (Figure S3). For instance, SH FeD emissions are estimated to be higher for the PD than for any other scenario due to higher surface winds simulated in this region. Interestingly, North African (and total) dust emission increases below low to moderate radiative forcing by the end of the century (SSPs 126 and 245) but it decreases at the highest forcing (SSP370).

The PI scenario is characterized by an insignificant anthropogenic influence, as a result FeF emissions are negligible (in line with the limited anthropogenic emissions in the CMIP6 inventory for year 1850). In the future, we find different directions depending on the scenario considered. SSP126 projects a decrease in FeF emissions compared to present day as a result of strong mitigation strategies (the emission budget is almost halved; 0.97 vs 1.75 Tg Fe/yr). The FeF global emission for scenario SSP245 is similar to the PD one (1.68 Tg Fe/yr), while for SSP370 a sharp increase in FeF emissions is

projected (3.11 Tg Fe/yr). In particular, FeF emissions are projected to drastically increase in East Asia for the SSP370 scenario. The estimated range of future FeF emissions (0.97-3.11 Tg Fe/yr) lies in good agreement with what other studies have used (Hamilton et al., 2020) (Table S2).

FeB emissions for the PI scenario do not contribute much to the total Fe emission (0.46 Tg Fe/yr). We note that CMIP6 PI fire emissions are inconsistent with the human-driven decline in burned area observed over the last century (Andela et al., 2017) and therefore are likely underestimated. Other datasets place PI FeB emissions between 3 and 5 times higher than our estimates. i.e, between 1.5 and 2.7 Tg Fe/yr (Hamilton et al., 2020). Projected FeB emissions decrease in the three future scenarios considered with 0.33, 0.38 and 0.47 Tg Fe/yr for SSP126, SSP245 and SSP370, respectively. FeB emissions are lower for all regions and scenarios (both past and future) compared to PD emissions, except for East Asia for the PI and SSP370 scenarios. Future projections of FeB emissions are ≈ 6 times lower than those used in Hamilton et al. (2020) based on RCP4.5 (CMIP5) scenario, as calculated in Ward et al. (2012). All in all, CMIP6 and other estimates are highly uncertain as the human-vegetation-fire-climate feedbacks are still not well understood. Multiple recent studies have tried to better constrain future fire emissions, but with diverging results (Yu et al., 2022; Kasoar et al., 2022).

3.2 OXL concentrations and aerosol acidity

OXL is fundamentally a secondary species, i.e., formed via chemical reactions in the atmosphere, and only a small fraction is directly emitted. PD OXL primary emissions are estimated to be 0.36 Tg OXL/yr. The trend in OXL emissions for past and future projections with respect to the PD follows FeB emissions (i.e., increase in emissions for PD compared to the PI and decrease of emissions for all future scenarios in comparison to PD, with sharper drop for the more optimistic scenario) (Figure S2). PD OXL net chemical production is 9.2 Tg OXL/yr, which is in the lower range of what has been reported in previous studies (Lin et al., 2014; Liu et al., 2012; Myriokefalitakis et al., 2021). The PI scenario shows a drop in the annual global mean OXL net chemical production compared to PD estimates. However, an increase is seen for SSP245 and SSP370 where OXL net chemical production is specially boosted over areas where anthropogenic activities are expected to increase (e.g., East Asia, South America and South Africa) (Figure 2).

Aerosol acidity is controlled by aqueous phase equilibria among inorganic species, such as sulphate, nitrate, ammonia and alkaline elements, e.g., calcium from mineral dust. Sulphate plays a key role in the system and is used here as proxy for aerosol acidity, Al-

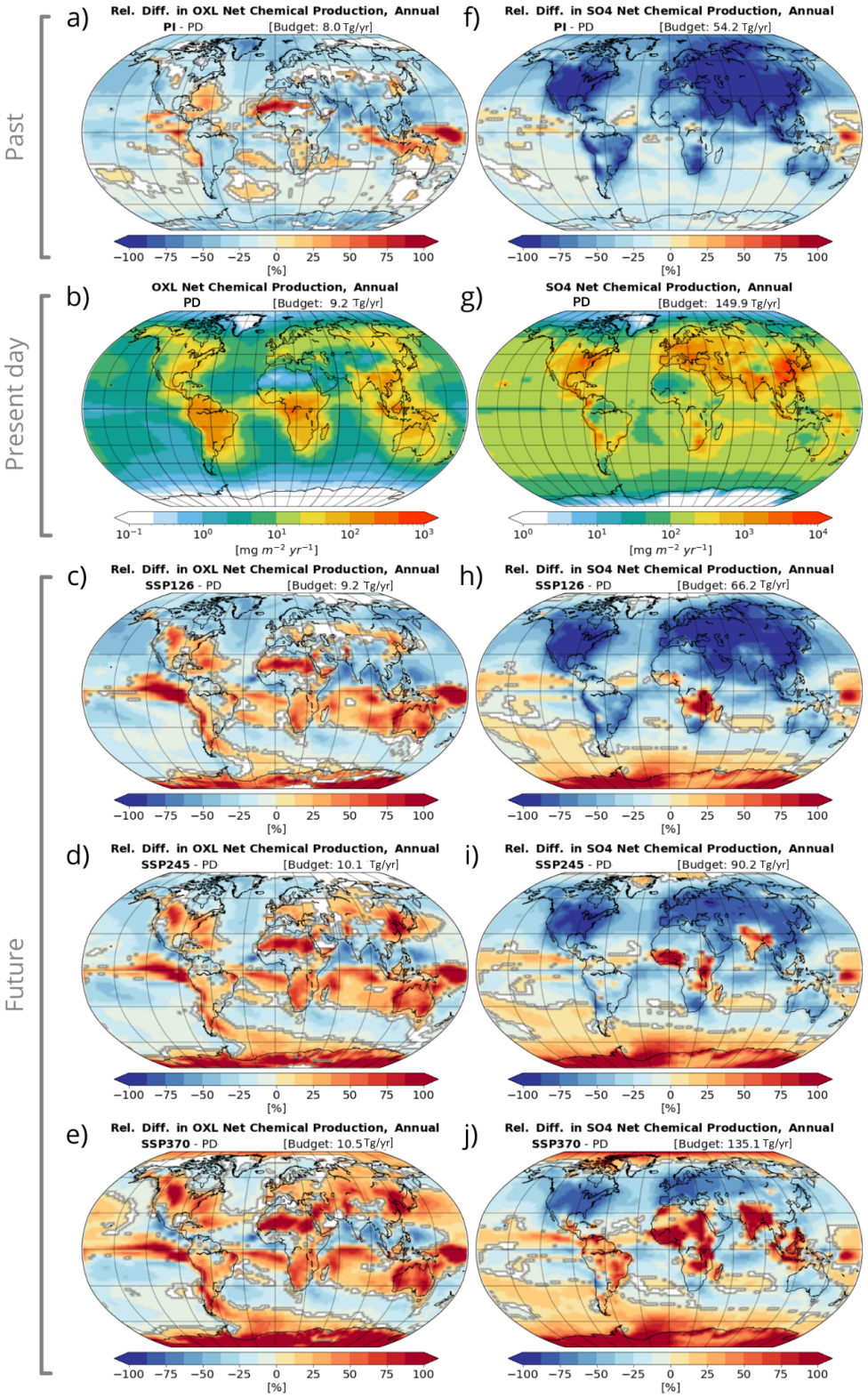

Figure 2. Mean annual PD net primary production of oxalate (b) and sulfate (g) (in Tg/yr) and relative differences between other scenarios fields and the PD (a,c,d,e for OXL and f,h,i,j for sulfate). The mean annual global chemical production budget is shown in brackets.

though emitted directly from some sources, sulphate is mostly formed in the atmosphere from gas-phase precursors, in particular SO_2. SO_2 emissions are 128 Tg SO_2/yr in the PD simulation, which represents a 9-fold increase over the PI period. SO_2 emissions dominated by the energy and industrial sector are expected to decrease overall as the energy sector gets decarbonized, with a more abrupt general decrease for SSP126 (i.e., the optimistic scenario, see Figure S2) (Gidden et al., 2019). This is true with the exception of some regions under the more pessimistic scenarios (e.g., the Middle East and Central Asia, North Africa and the SH for SSP370) where an increase in the industrial demand is hypothesized (Figure S2). SO_4^{2-} net chemical production for PD is 149.9 Tg SO_4^{2-}/yr and follows the trends seen in SO_2 emissions; a 2.8-fold increase in PD estimates is seen compared with the PI while a decrease is projected for all three future scenarios especially in the Northern Hemisphere (NH) (Figure 2)

Aerosol pH and OXL concentrations, which are key to understanding Fe solubilization, present notable differences among scenarios (Figure 3). Mean aerosol pH values are the lowest (i.e., more acidic) during the PD period, both in the accumulation and coarse modes, 2.15 and 3.79, respectively. The PI scenario, with a more pristine atmosphere, is the scenario presenting higher pH values (i.e., less acidic), 2.36 and 4.37 as global means for accumulation and coarse modes. Projections follow the SO_2 emission and SO_4^{2-} net chemical production trends discussed above, with the scenario representing a more sustainable pathway (SSP126) showing acidity values closer to PI estimates, 2.36 and 4.21, and the scenario with higher prescribed anthropogenic emissions (SSP370) showing values closer to the ones in the PD, 2.18 and 3.88 global pH means for accumulation and coarse modes, respectively.

The accumulation mode is in general more acidic in all scenarios, specially over the tropical ocean, where values close to 1 are reached. In dusty regions, like North Africa, the lower concentrations of anthropogenic aerosols and the high concentrations of buffering minerals like calcite lead to less acidic conditions (Figure 3a-j). In the coarse mode, slightly acidic pH values are simulated over ocean, whereas over continental regions the pH is lower (i.e., close to 1), particularly where anthropogenic activity is intense. Regionally, our scenarios project an increase in acidity over developing regions (e.g., Africa, South America and the Middle East and Asia), where population and energy and industry requirements are expected to grow in the near future, specially under SSP370.

Present-day estimates of OXL (Figure 3l) show maximum surface concentrations over major biomass burning sources such as Central Africa, South America and Indonesia, as well as OXL net chemical production (Figure 2b), but also downwind of those sources (up to 0.2 $\mu g/m^3$ on annual average) and decrease steeply towards the poles. Overall,

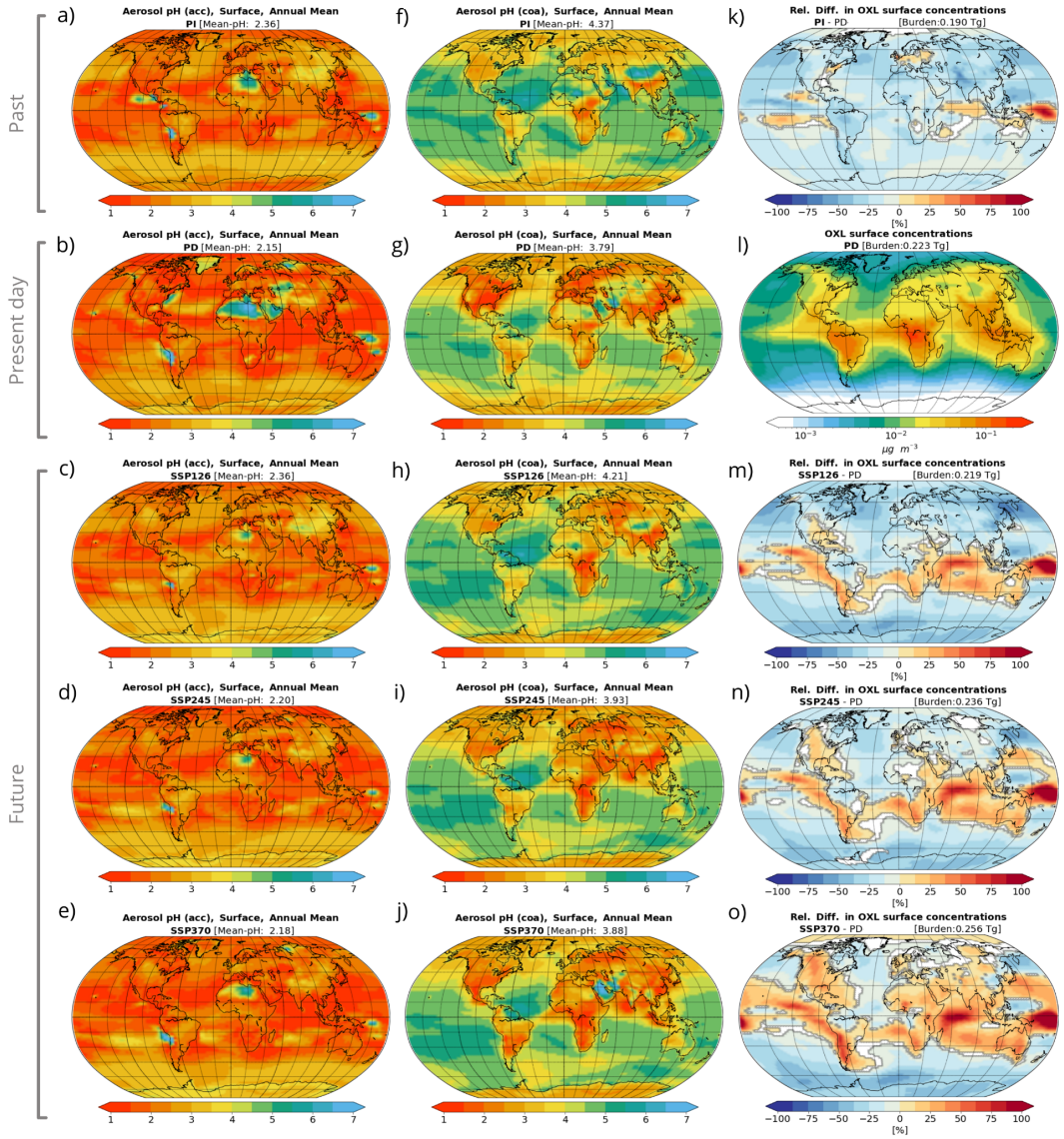

Figure 3. Surface aerosol pH for the accumulation (left column, a-e) and coarse modes (middle column, f-j) of the model for all considered scenarios (PI, PD, SSP126, SSP245 and SSP370, from top to bottom). Mean (area-weighted) pH values are shown for each scenario and mode. OXL surface concentration for the PD scenario (l) and relative differences [in %] of other scenarios compared to the PD one (right column; k,m,n,o). Mean annual OXL budget values are shown for each scenario and mode in Tg.

lower concentrations are found in the PI, with relative decreases between 10 and 30%, with except in certain equatorial regions of the Indian and Pacific Ocean, and Europe (Figure 3k), where up to 100% higher concentrations are found. In the future projections, OXL sharply increases in the Indian Ocean and equatorial Pacific. Also, OXL is expected to increase over and downwind of South Africa, southern South America and Australia. Under SSP370, the increases extend over other areas such as the North American continent, North Africa and the Asian and European continent. As OXL has mostly a secondary origin, changes in OXL surface concentrations between simulations are fundamentally driven by changes in OXL net chemical production (Figure 2a-e), which ultimately depends on the abundance of organic precursors.

3.3 Atmospheric Fe solubilization

Fe at emission is considered to be mostly insoluble; in EC-Earth3-Iron only 0.1% of the emitted FeD and 80% of the emitted Fe from shipping emissions are assumed to be soluble. In this section, FeF and FeB are discussed together as Fe from those sources are considered to have the same dissolution rates and treated in the EC-Earth3-Iron solubilization scheme as one pool (FeC) (Section 2.1.1). For the PD, SFe emissions are 0.0425 and 0.00011 Tg/yr for FeD and FeC emissions, respectively. Additionally, 0.473 $\pm$ 0.013 Tg FeD/yr and 0.284 $\pm$ 0.016 Tg FeC/yr are dissolved in the atmosphere.

All in all, around 95% of atmospheric SFe results from atmospheric dissolution processes. FeD is primarily dissolved by acid dissolution, with a rate of 0.296 $\pm$ 0.007 Tg FeD/yr. Ligand-promoted dissolution additionally produces 0.138 $\pm$ 0.010 Tg FeD/yr and photo-induced processes have a small impact on the global dissolved Fe release from dust, with 0.039 $\pm$ 0.003 Tg FeD/yr (Figure 4). On the other hand, the main dissolution path for FeC is ligand-promoted dissolution with a rate of 0.189 $\pm$ 0.004 Tg Fe/yr. Acidic and photo-induced dissolution each represent 17% of the FeC dissolution, with rates of 0.0478 $\pm$ 0.0011 Tg Fe/yr and 0.0476 $\pm$ 0.0011 Tg Fe/yr, respectively (Figure 4). Ligand-promoted dissolution is the main solubilization pathway for FeC in our model, in agreement with results from experimental studies showing fast dissolution rates (Chen & Grassian, 2013). This pathway is further fostered by the combustion activities emitting both FeC and OXL precursors, which results in the maximum values of OXL production (Figure 2b) being spatially correlated with high solubilization values of FeC (Figure S4a-f) .

Dissolution rates of FeC are 65% smaller in the PI scenario than in the PD. FeD dissolution is also smaller in the PI scenario, by 65% the acidic dissolution and by 20% the OXL-promoted and photo-induced dissolution. The drop in Fe dissolution is mainly

driven by a reduction in direct FeC emissions (75%) (Figure 1) and a drop in OXL and SO_4^{2-} net chemical production (≈13% and ≈64% respectively) (Figure 2).

Different trends can be seen on our future scenarios of Fe dissolution compared to the PD. On the one hand, SSP126 shows a decrease in atmospheric Fe processing for both FeD and FeC, specially due to reduced acidic dissolution. Although FeD emissions in this scenario are 12.5% higher than in the PD, there is a relative reduction of nearly 60% in FeD acidic dissolution. The decrease is mainly driven by the drop in SO_2 emissions (Figure S2), leading to a less acidic atmosphere (Figure 3c and 3h). On the other hand, SSP245 estimates a 12% increase in OXL-promoted and photoinduced Fe dissolution, and a relative decrease of 26% in Fe acidic dissolution. The drop in proton-promoted dissolution is driven by a decrease in aerosol acidity, specially over dust sources and areas downwind (Figure 3). The increase in OXL over some equatorial regions, where FeF emissions are projected to increase, leads to an enhanced ligand-promoted dissolution (Figure S2d). In SSP370, the scenario with higher NTCF levels projected, Fe dissolution increases for both FeD and FeC as a result of all processing mechanisms. The increase in FeC solubilization is especially abrupt compared to the PD, with values ranging between 91 and 98 % more for the different mechanisms. This results from a 78 % increase in FeF primary emissions relative to PD (Figure 1), together with an OXL production increase around anthropogenic sources, and a significant increase in coarse aerosol acidity in Southern Asia, the Middle East and the Gulf of Guinea.

No substantial differences are seen when comparing the global solubilization budgets of the SSP370 scenarios with regionally perturbed dust emission with the base SSP370 simulation (Figure S5). Despite the large increase in global FeD emissions in some experiments, i.e., SSP370-NAfr (≈ ×2), SSP370-EAsia (≈ ×1.3) and SSP370-MEast (≈ ×1.2), minor changes are seen in Fe solubilization budgets. This is explained by the increase in calcium carbonate, which buffers acidity and therefore limits FeD solubilization (Myriokefalitakis et al., 2021).

3.4 Soluble iron deposition and solubility

The Fe deposition in our PD scenario is 42 ± 5 Tg Fe/yr, with 12.1 ± 1.4 Tg Fe/yr deposited to the ocean. The SFe deposition is 0.721 ± 0.018 Tg SFe/yr, with 0.406 ± 0.011 Tg SFe/yr deposited to the ocean (Figure 5). 70% of SFe deposited in the ocean comes from dust mineral sources, while the remaining 14 and 16 % come from anthropogenic combustion and biomass burning sources, respectively. Since FeD emissions represent ≈ 95% of total Fe emissions (99.7% of directly SFe emissions), these results reflect the stronger atmospheric processing of FeC compared to FeD in present day con-

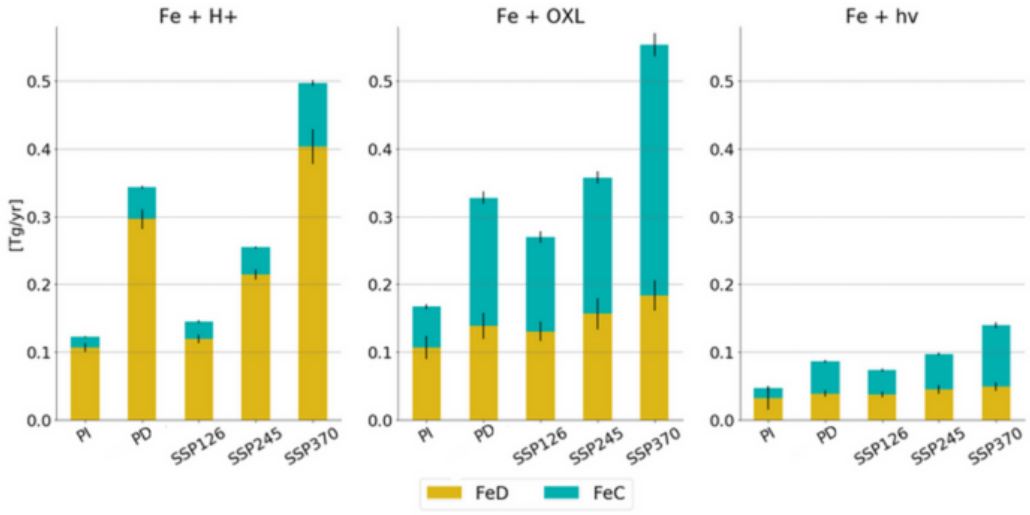

Figure 4. Fe solubilization budgets for the different scenarios and atmospheric processing mechanisms: acidic dissolution (left), oxl-promoted dissolution (middle), and photoreductive dissolution budgets (right). Solubilization of Fe from dust sources (FeD) is represented with the yellow-orange colour and solubilization of Fe from combustion sources (FeC) (i.e., both from biomass burning, FeB, and anthropogenic sources, FeF) is represented in blue-green colour. Black bars indicate the budget spread for the 30 ensemble members.

ditions. As discussed in Section 3.3, this is due mainly to enhanced OXL-promoted dissolution in combustion aerosols. Our Fe and SFe deposition budgets in the ocean along with contribution of each source to the total deposition are within the range of previous studies (Figure 5 and Table S1) (Hamilton et al., 2020, 2019; Ito et al., 2019; Ito & Shi, 2016; M. S. Johnson & Meskhidze, 2013; Luo & Gao, 2010; Luo et al., 2008; Myriokefalitakis, Gröger, et al., 2020; Myriokefalitakis et al., 2018, 2015; Scanza et al., 2018).

Total Fe deposition budgets do not present significant differences among scenarios (Figure 5a), ranging between 42 and 47 Tg Fe/yr, and 11 and 13 Tg Fe/yr over the oceans. This follows from Fe emission shown in Figure 1 being dominated by dust, whose global emission shows small variations between the scenarios. In contrast, SFe deposition budgets do show substantial variations among scenarios with the lowest values reached in the PI, with 0.377 $\pm$ 0.015 Tg SFe/yr globally and 0.209 $\pm$ 0.009 Tg SFe/yr over ocean. Our PI SFe deposition compares well with prior studies (Figure 5b), with the exception of Hamilton et al. (2020) in which SFe deposition over the ocean more than doubles our estimates, most likely due to the use of a different fire emission dataset (Hamilton et al., 2018). A decline in SFe deposition is observed for the SSP126 and SSP245 scenarios com-

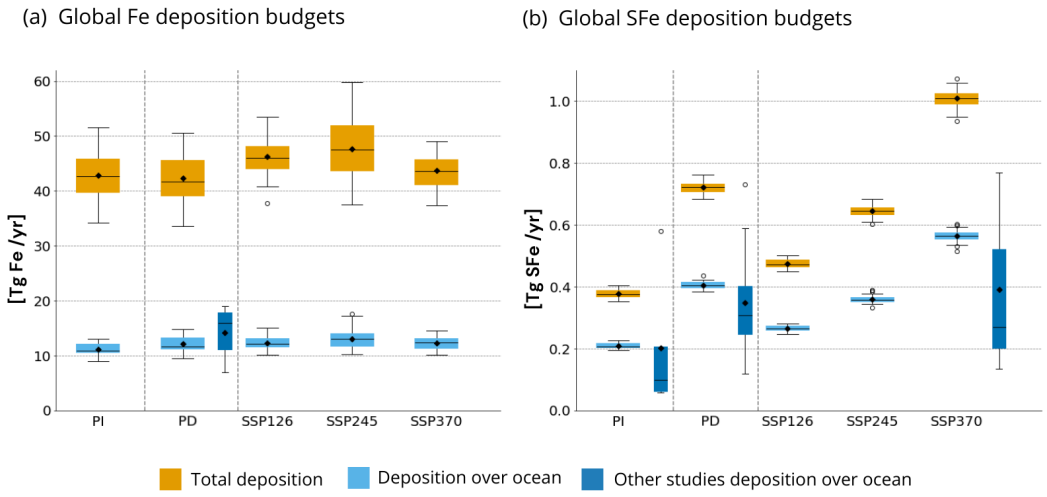

Figure 5. (a) Global total Fe deposition budgets (in orange, global deposition, in light-blue, deposition over ocean) for all our scenarios (b) Global SFe deposition budgets (in blue only deposition over ocean) for all our scenarios. Dark-blue boxes are built up from literature data (Table S1).

pared to PD, with 0.474 ± 0.013 Tg SFe/yr (0.265 ± 0.009 Tg SFe/yr) globally (over ocean) for SSP126, and 0.646 ± 0.019 Tg SFe/yr (0.360 ± 0.013 Tg SFe/yr) for SSP245. The projected reductions under these two scenarios are consistent with the drop in atmospheric Fe solubilization (Section 3.3). SSP370 scenario shows a clear increase in SFe deposition in comparison to all other scenarios, with 1.01 ± 0.03 Tg SFe/yr (0.56 ± 0.02 Tg SFe/yr) globally (over ocean). SFe deposition increases with increasing NTCF, and is almost doubled for SSP370 with respect to SSP126, while the SSP245 deposition falls in the middle. Although there are not many studies dealing with Fe deposition in the future, we can see that the estimates of our different scenarios also fall in the range of previous literature (Table S1).

PD estimates show maximum values of SFe deposition near the equatorial Atlantic downwind of dust mineral and biomass burning sources, and the north coast of the Indian Ocean where Fe comes from dust mineral sources and anthropogenic combustion (Figure 6b). In HNLC regions, such as the SO, the SFe deposition is lower than over the rest of the globe. The maximum solubility of Fe (i.e., the fraction of SFe over total Fe) at deposition (≈ 20 %) occurs downwind of South African biomass burning sources, East Asian anthropogenic combustion sources, and remote equatorial regions of the Pacific, dominated by long-range transport of dust (Figure 6g). The higher solubility of Fe de-

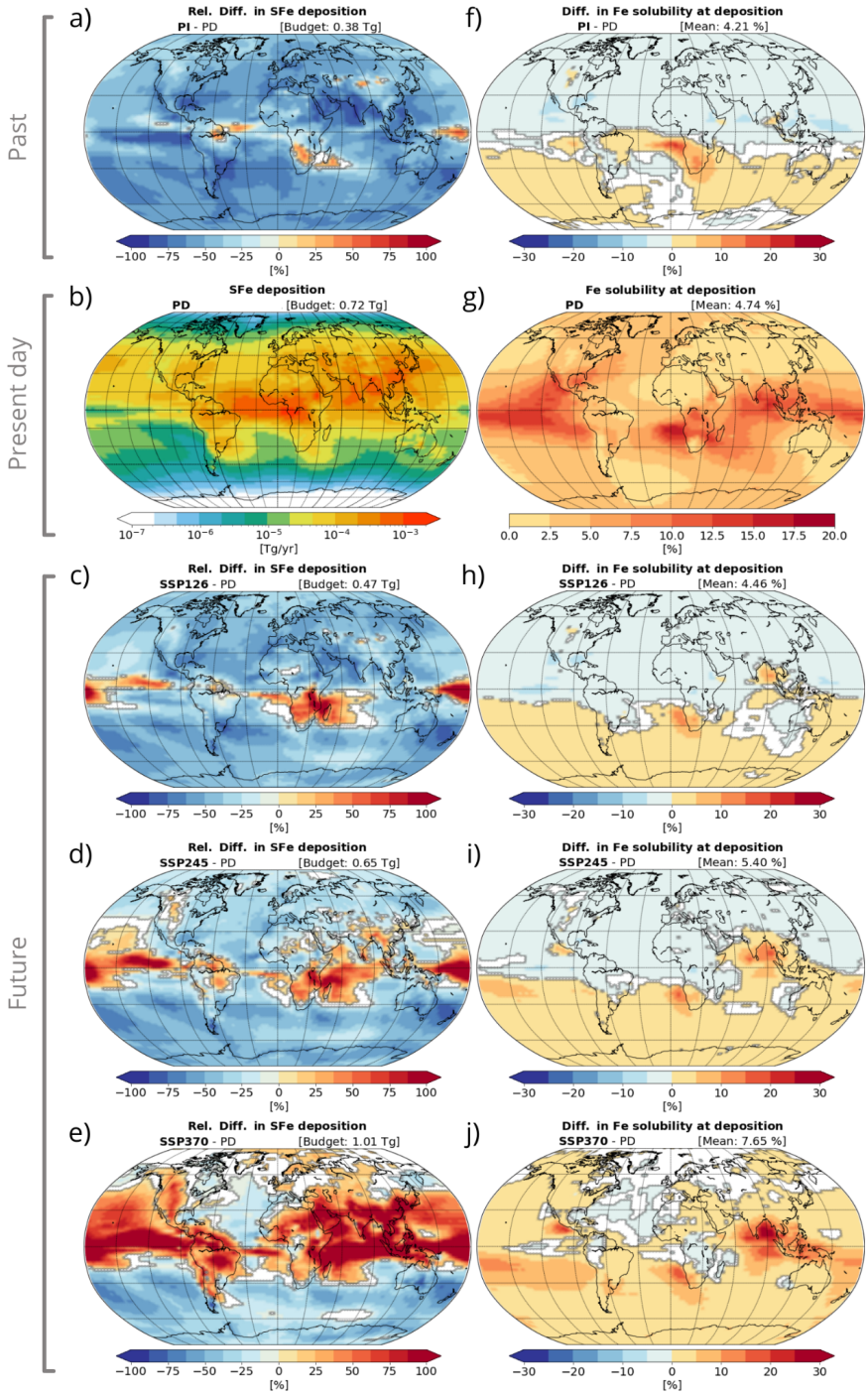

Figure 6. Mean SFe deposition (in Tg SFe/yr) for the PD scenario (b) and relative differences between other scenarios and the PD (left column; a,c,d,e), Fe solubility at deposition (in %) for the PD scenario (g) and absolute differences compared to other scenarios (right column; f,h,i,j). Mean annual SFe deposition budgets and mean solubility values are shown in the respective maps.

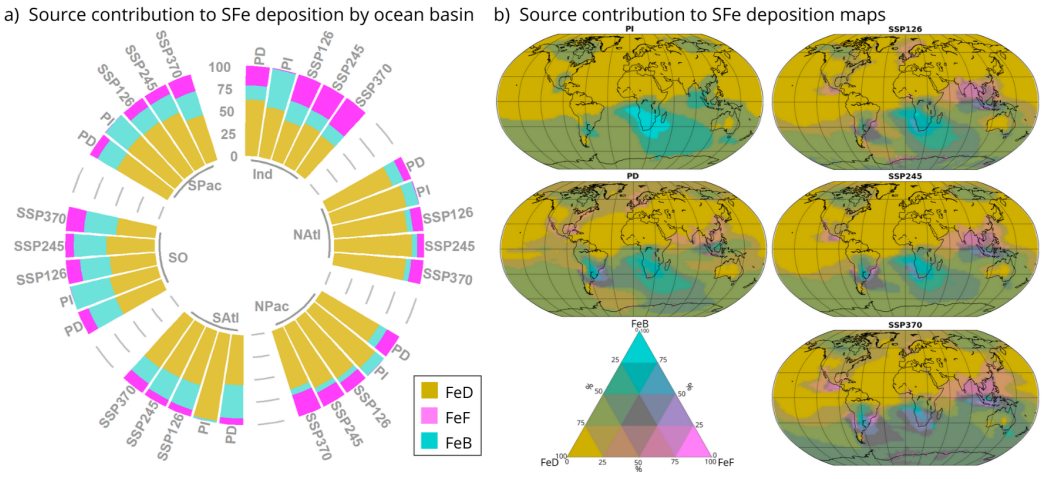

Figure 7. a) Source contribution (%) to SFe deposition by ocean basin. Yellow indicates Fe from dust sources (FeD), pink, Fe from fossil fuels (FeF) and blue, Fe from biomass burning sources (FeB). b) Contribution of each source to the SFe deposition flux at each grid cell where pure yellow indicates that ≈ 100 % of deposited SFe comes from mineral dust, pure pink indicates ≈ 100 % of deposited SFe comes from anthropogenic combustion and pure blue shows that ≈ 100 % of deposited SFe comes from biomass burning; other colours represent the different mixtures of sources.

posited over ocean compared to land is attributed to the longer lifetime of Fe-aerosols reaching the ocean, being thus more exposed to atmospheric processing. The PI scenario shows globally lower SFe deposition than the PD, except for some areas like South Africa (Figure 6a) where higher biomass burning emissions affect the solubility levels. Future scenarios show a decrease in SFe deposition in mid- and high-latitudes, but an increase in equatorial regions such as the equatorial Pacific, Atlantic and Indian Ocean. Those increases are sharper and have a broader extension for SSP370, which is the future scenario with higher FeF emissions, aerosol acidity and OXL concentrations (Figure 6e). Solubility increases only in the SO and some regions of the Indian Ocean (e.g., the Bay of Bengal) for SSP126 and SSP245, while for SSP370 solubility increases in all regions but the North Atlantic. The increase in solubility for future scenarios could be driven by a change in Fe source contribution, likely related to a higher contribution of more labile Fe sources such as biomass burning and anthropogenic combustion. Those differences are reflected in the source contribution to SFe deposition for the different scenarios (Figure 7). In line with the emissions, the contribution of anthropogenic sources to SFe deposition is negligible, but the contribution from biomass burning sources is particularly high, specially in the SH. Overall, the NH SFe deposition is dominated by dust

in all scenarios, although in some areas, such as the North Pacific or the North Indian Ocean, there is an increase in anthropogenic contribution for future scenarios, specially for SSP370. Moreover, for SSP370 the dust contribution is below 50% for the Indian and SO, which does not happen in any other scenario and basin.

Doubling dust emissions per region under SSP3-7.0 conditions causes a slight increase in global SFe deposition independently of the perturbed region, except for the North American sources, which does not induce any significant changes (Figure 8a-d). However, those increases are more relevant in some regions specially downwind the perturbed sources. Perturbing North African dust sources causes a broader impact than changes in any other source, and leads to relative increases of up to 25% in SFe deposition with respect to the baseline SSP370 scenario in remote regions of the SH. In particular, our model shows that SFe deposition in HNLC regions, such as the SO and the equatorial Pacific, is sensitive not only to changes in Australian or South American dust sources, but also to changes in North African sources. On the other hand, solubility decreases in regions close to the perturbed sources in all scenarios considered. This is something expected when increasing dust emissions for two main reasons. On the one hand, we are increasing the contribution of dust sources to Fe deposition, and FeD is known to be solubilized at slower rates than FeF or FeB. In addition, as explained above, more dust (and therefore calcium carbonate) buffers the acidity, which limits solubilization.

4 Conclusions

Changes in climate and emissions can substantially modify atmospheric aerosol acidity, OXL production, and the strength and distribution of SFe deposition. Estimating these changes is crucial to assess future marine productivity and carbon and nitrogen cycles. Here, we have characterized the past, present and potential future SFe deposition with an ESM (EC-Earth3-Iron) that is equipped with a detailed representation of atmospheric Fe dissolution (Myriokefalitakis et al., 2021). In this way, the SFe deposition in EC-Earth3-Iron is expected to respond more realistically to changes in climate and emissions. Our experimental setup covers the PI period, the PD, and a range of possible future climates following different CMIP6 emission scenarios. These scenarios cover from substantially reduced anthropogenic emissions, associated with very ambitious mitigation strategies, to large increases in emissions related to a growing population, especially in low- and middle-income countries, and a resurgence of coal dependence. Our new model capabilities allow us to predict not only iron from different sources (FeD, FeF, and FeB) but also the precursors and processes controlling iron dissolution explicitly and interactively under changing climate conditions and emission levels.

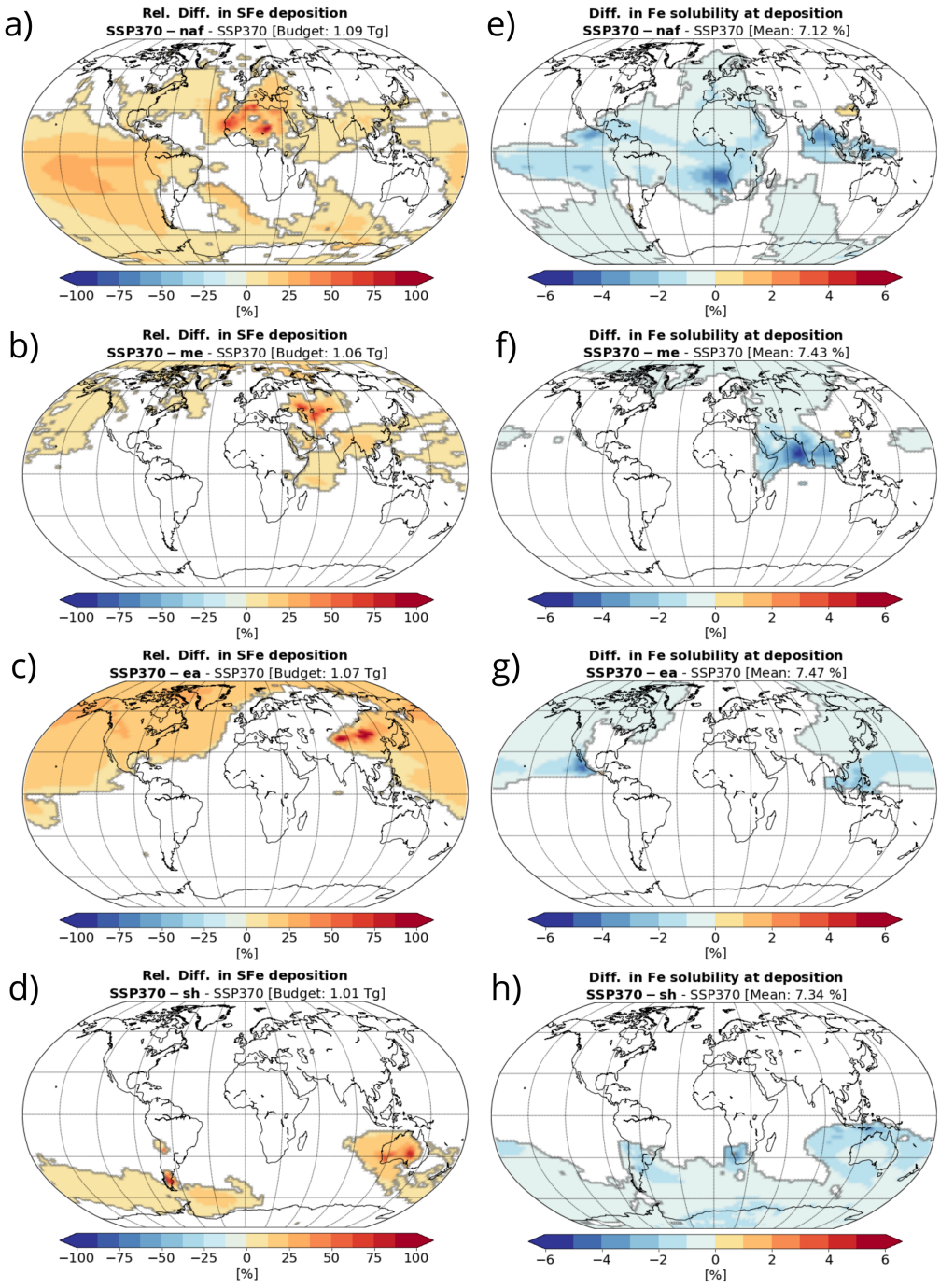

Figure 8. Relative differences between SFe deposition of SSP370 perturbed dust scenarios and SSP370 base scenario (left column). Absolute differences in Fe solubility at deposition (%) between SSP370 perturbed dust scenarios and SSP370 base scenario (right column). From first to last row the regions perturbed are: North Africa (NAfr), Middle East (MEast), East Asia (EAsia) and Southern Hemisphere (SH). Mean SFe deposition budgets and solubilities are shown within each scenario.

According to our calculations, the SFe deposition to the ocean has doubled since the early PI (0.406 ± 0.011 Tg SFe/yr and 0.209 ± 0.009 Tg SFe/yr respectively), in agreement with some previous studies (Hamilton et al., 2020; Ito & Shi, 2016; Myriokefalitakis et al., 2015). We project an increase in global SFe deposition of 40% by the late 21st century relative to PD under the low mitigation scenario SSP370, and a decrease of 35 and 11% under the optimistic SSP126 and business-as-usual SSP245 scenarios, respectively. This is in line with the trends showed in aerosol acidity and OXL levels: low acidity (high pH) and concentrations of OXL in the PI and increases in both for SSP370 specially close to developing countries. In all scenarios, total Fe emissions are dominated by dust sources with a contribution above 90%. Dust sources dominate as well SFe global deposition, but the contribution of FeC aerosols to SFe ($\approx 30\%$ during the PD) is enhanced relative to emissions as atmospheric processing is especially efficient for FeC aerosols. We find that in all scenarios, ligand-promoted dissolution is the main FeC solubilization pathway and proton-promoted dissolution is the main one for FeD.

Dust sources dominate SFe deposition in the Northern hemisphere and globally. However, biomass burning and anthropogenic combustion emissions have a more crucial role in the SH. Anthropogenic combustion emissions do not contribute during the PI, but show significant contributions in the PD and future scenarios over the East Asian coast, Central American coast, and part of the South American region. SSP370 is the future scenario with the highest contribution of anthropogenic combustion sources to SFe deposition (especially in the Indian ocean). Biomass burning emissions dominate along the Southern African coast for all scenarios, especially in the PI. This shows that although dust sources are dominant, combustion sources are not at all negligible in regions such as the SO, known to be HNLC regions.

Our results suggest potentially large differences in the ocean response among future scenarios. However, there are patterns shared among all future scenarios that could have important implications for the ability of the ocean to capture carbon in the future. In all future scenarios, we obtain a decrease in SFe deposition over the Fe-limited SO, and an increase over the equatorial Pacific, also known as a HNLC region. The net effect of these changes in the global carbon capture is uncertain. Further analyses are planned where we will use our SFe deposition fields in a biogeochemistry model to understand the regional and global ocean productivity changes associated with future scenarios.

Past and future projected emissions are very uncertain and need further investigation. Recent studies suggest that CMIP6 probably underestimates PI fire emissions (Hamilton et al., 2019), and others also suggest large uncertainties in future fire emission estimates (Yu et al., 2022; Kasoar et al., 2022). Uncertainties in fire emissions also

affect the burden of precursors of OXL and therefore Fe dissolution. Potential changes in the spatial extent of dust sources due to changes in vegetation (Mahowald, 2007), land use (Ginoux et al., 2012), and biocrusts (Rodriguez-Caballero et al., 2022) are either poorly considered or not considered at all in ESMs. As seen in our perturbed dust experiments, HNLC regions such as the SO and equatorial Pacific could be very sensitive to those changes in dust emissions. Dust emissions associated with wildfires, where strong, turbulent fire-related winds most likely raise dust (Hamilton et al., 2022; Wagner et al., 2018), are largely disregarded in current models. Additionally, by destroying vegetation, wildfires leave a bare source that often becomes a source of dust emission (Yu & Ginoux, 2022). Variations in these climate-sensitive, yet unaccounted, emissions could alter SFe deposition. Future observational and modelling studies should focus on better characterizing the evolution of fire and dust emissions and its interaction with other Earth System components to ultimately better represent the Fe cycle.

Acknowledgments

This work was funded by the European Research Council under the Horizon 2020 research and innovation programme through the ERC Consolidator Grant FRAGMENT (grant agreement No. 773051), the AXA Research Fund through the AXA Chair on Sand and Dust Storms at BSC, the Spanish Ministerio de Economía y Competitividad through the NUTRIENT project (CGL2017-88911-R), the European Union's Horizon 2020 research and innovation programme under grant agreement No 821205 (FORCeS), and ESA through the DOMOS project (ESA AO/1-10546/20/I-NB).

We acknowledge the EMIT project, which is supported by the National Aeronautics and Space Administration Earth Venture Instrument program, under the Earth Science Division of the Science Mission Directorate. RLM received additional support from the NASA Modeling, Analysis and Prediction Program (NNG14HH42I). We also acknowledge the resources obtained on the Marenostrum4 supercomputer at BSC, granted through the PRACE project eFRAGMENT2 and RES project AECT-2020-3-0020, along with the technical support provided by BSC and the Computational Earth Sciences team of the BSC Earth Sciences Department. We also thank Pablo Ortega, Markus Donat and Ettiene Tourigny from the Climate Variability and Change team of the BSC Earth Sciences Department for their recommendations on the experimental setup. We further acknowledge the EC-Earth community and the AerChemMIP team. We thank the climate modelling groups for producing and making available their model output, the Earth System Grid Federation (ESGF) for archiving the data and providing access, and the multiple funding agencies that support CMIP6 and ESGF.

Elisa Bergas-Massó: Conceptualization, Methodology, Software, Formal analysis, Writing - Original Draft, Visualization **María Gonçalves Ageitos**: Conceptualization, Methodology, Writing - Review & Editing, Supervision, Project administration, Funding acquisition **Stelios Myriokefalitakis**: Conceptualization, Methodology, Software, Writing - Review & Editing, Supervision **Ron L. Miller**: Writing - Review & Editing **Twan van Noije**: Software, Writing - Review & Editing **Philippe Le Sager**: Software **Gilbert Montané Pinto**: Software **Carlos Pérez García-Pando**: Conceptualization, Methodology, Resources, Writing - Review & Editing, Supervision, Project administration, Funding acquisition

Open Research

The EC-Earth3-Iron code is available from the EC-Earth development portal (https://dev.ec-earth.org/) for members of the EC-Earth consortium. Model codes developed at the European Centre for Medium-Range Weather Forecasts (ECMWF), such as the IFS model code, are intellectual property of ECMWF and its member states. Permission to access the EC-Earth3-Iron source code can be requested from the EC-Earth community via the EC-Earth website (http://www.ec-earth.org/) and may be granted if a corresponding software license agreement is signed with ECMWF. The corresponding repository tag is 3.3.2.1-Fe. Due to license limitations of the model, only European users can be granted access.

Other data used in this study will be available in the open repository Zenodo upon acceptance of the manuscript.

References

Andela, N., Morton, D. C., Giglio, L., Chen, Y., Van Der Werf, G. R., Kasibhatla, P. S., ... Randerson, J. T. (2017). A human-driven decline in global burned area. *Science*, *356*(6345), 1356–1362. doi: 10.1126/science.aal4108

Baker, A. R., & Croot, P. L. (2010). Atmospheric and marine controls on aerosol iron solubility in seawater. *Marine Chemistry*, *120*(1-4), 4–13. doi: 10.1016/j.marchem.2008.09.003

Baker, A. R., Jickells, T. D., Witt, M., & Linge, K. (2006, 01). Trends in the solubility of iron, aluminium, manganese and phosphorus in aerosol collected over the atlantic ocean. *Marine Chemistry*, *98*, 43-58. doi: 10.1016/j.marchem.2005.06.004

Behrenfeld, M., O'Malley, R., Siegel, D., Mcclain, C., Sarmiento, J., Feldman, G., ... Boss, E. (2007, 01). Climate-driven trends in contemporary ocean productivity.

In *Nature* (Vol. 444, p. 752-5).

Boyd, P. W., Strzepek, R., Takeda, S., Jackson, G., Wong, C. S., McKay, R. M., ... Ramaiah, N. (2005). The evolution and termination of an iron-induced mesoscale bloom in the northeast subarctic Pacific. *Limnology and Oceanography*, *50*(6), 1872–1886. doi: 10.4319/lo.2005.50.6.1872

Carlton, A. G., Turpin, B. J., Altieri, K. E., Seitzinger, S., Reff, A., Lim, H.-J., & Ervens, B. (2007, nov). Atmospheric oxalic acid and SOA production from glyoxal: Results of aqueous photooxidation experiments. *Atmospheric Environment*, *41*(35). doi: 10.1016/j.atmosenv.2007.05.035

Chen, H., & Grassian, V. H. (2013). Iron dissolution of dust source materials during simulated acidic processing: The effect of sulfuric, acetic, and oxalic acids. *Environmental Science and Technology*, *47*(18), 10312–10321. doi: 10.1021/es401285s

Chuang, P. Y., Duvall, R. M., Shafer, M. M., & Schauer, J. J. (2005). The origin of water soluble particulate iron in the asian atmospheric outflow. *Geophysical Research Letters*, *32*(7). doi: 10.1029/2004GL021946

Ciais, P., Sabine, C., Bala, G., Bopp, L., Brovkin, V., Canadell, J., ... Thornton, P. (2013). Carbon and other biogeochemical cycles. In T. Stocker et al. (Eds.), *Climate change 2013: The physical science basis. contribution of working group i to the fifth assessment report of the intergovernmental panel on climate change.* Cambridge University Press, Cambridge, United Kingdom and New York, NY, USA.

Claquin, T., Schulz, M., & Balkanski, Y. (1999, 09). Modeling the mineralogy of atmospheric dust sources. *Journal of Geophysical Research*, *104256*, 243-22. doi: 10.1029/1999JD900416

Desboeufs, K. V., Losno, R., Vimeux, F., & Cholbi, S. (1999, sep). The pH-dependent dissolution of wind-transported Saharan dust. *Journal of Geophysical Research: Atmospheres*, *104*(D17). doi: 10.1029/1999JD900236

Döscher, R., Acosta, M., Alessandri, A., Anthoni, P., Arneth, A., Arsouze, T., ... Zhang, Q. (2021). The EC-Earth3 Earth System Model for the Climate Model Intercomparison Project 6. *Geoscientific Model Development Discussions*, *2021*, 1–90. doi: 10.5194/gmd-2020-446

Duce, R. A., & Tindale, N. W. (1991, dec). Atmospheric transport of iron and its deposition in the ocean. *Limnology and Oceanography*, *36*(8). doi: 10.4319/lo.1991.36.8.1715

EPICA, c. m. (2004). Eight glacial cycles from an Antarctic ice core. *Nature*, *429*(6992), 623–628. doi: 10.1038/nature02599

Eyring, V., Bony, S., Meehl, G. A., Senior, C. A., Stevens, B., Stouffer, R. J., & Taylor, K. E. (2016). Overview of the Coupled Model Intercomparison Project Phase 6 (CMIP6) experimental design and organization. *Geoscientific Model Development*, *9*(5), 1937–1958. doi: 10.5194/gmd-9-1937-2016

Fountoukis, C., & Nenes, A. (2007). ISORROPIAII: A computationally efficient thermodynamic equilibrium model for K+-Ca2+-Mg2+-NH4+-Na+-SO42–NO3–Cl–H2O aerosols. *Atmospheric Chemistry and Physics*, *7*(17), 4639–4659. doi: 10.5194/acp-7-4639-2007

Gates, W. L., Boyle, J. S., Covey, C., Dease, C. G., Doutriaux, C. M., Drach, R. S., ... Williams, D. N. (1999). An Overview of the Results of the Atmospheric Model Intercomparison Project (AMIP I). *Bulletin of the American Meteorological Society*, *80*(1), 29–55. doi: 10.1175/1520-0477(1999)080⟨0029:AOOTRO⟩2.0.CO;2

Gidden, M. J., Riahi, K., Smith, S. J., Fujimori, S., Luderer, G., Kriegler, E., ... Takahashi, K. (2019, apr). Global emissions pathways under different socioeconomic scenarios for use in CMIP6: a dataset of harmonized emissions trajectories through the end of the century. *Geoscientific Model Development*, *12*(4). doi: 10.5194/gmd-12-1443-2019

Ginoux, P., Prospero, J. M., Gill, T. E., Hsu, N. C., & Zhao, M. (2012, sep). Global-scale attribution of anthropogenic and natural dust sources and their emission rates based on MODIS Deep Blue aerosol products. *Reviews of Geophysics*, *50*(3). doi: 10.1029/2012RG000388

Gliß, J., Mortier, A., Schulz, M., Andrews, E., Balkanski, Y., Bauer, S. E., ... Tsyro, S. G. (2021). AeroCom phase III multi-model evaluation of the aerosol life cycle and optical properties using ground- And space-based remote sensing as well as surface in situ observations. *Atmospheric Chemistry and Physics*, *21*(1), 87–128. doi: 10.5194/acp-21-87-2021

Guieu, C., Bonnet, S., Wagener, T., & Loÿe-Pilot, M.-D. (2005). Biomass burning as a source of dissolved iron to the open ocean? *Geophysical Research Letters*, *32*(19). doi: 10.1029/2005GL022962

Hajima, T., Watanabe, M., Yamamoto, A., Tatebe, H., Noguchi, M., Abe, M., ... Kawamiya, M. (2019). Description of the MIROC-ES2L Earth system model and evaluation of its climate–biogeochemical processes and feedbacks. *Geoscientific Model Development*. doi: 10.5194/gmd-2019-275

Hamilton, D. S., Hantson, S., Scott, C. E., Kaplan, J. O., Pringle, K. J., Nieradzik, L. P., ... Carslaw, K. S. (2018, dec). Reassessment of pre-industrial fire emissions strongly affects anthropogenic aerosol forcing. *Nature Communications*,

9(1). doi: 10.1038/s41467-018-05592-9

Hamilton, D. S., Moore, J. K., Arneth, A., Bond, T. C., Carslaw, K. S., Hantson, S., ... Mahowald, N. M. (2020, mar). Impact of Changes to the Atmospheric Soluble Iron Deposition Flux on Ocean Biogeochemical Cycles in the Anthropocene. *Global Biogeochemical Cycles*, *34*(3). doi: 10.1029/2019GB006448

Hamilton, D. S., Perron, M. M., Bond, T. C., Bowie, A. R., Buchholz, R. R., Guieu, C., ... Mahowald, N. M. (2022). Earth, Wind, Fire, and Pollution: Aerosol Nutrient Sources and Impacts on Ocean Biogeochemistry. *Annual Review of Marine Science*, *14*, 303–330. doi: 10.1146/annurev-marine-031921-013612

Hamilton, D. S., Scanza, R. A., Feng, Y., Guinness, J., Kok, J. F., Li, L., ... Mahowald, N. M. (2019, sep). Improved methodologies for Earth system modelling of atmospheric soluble iron and observation comparisons using the Mechanism of Intermediate complexity for Modelling Iron (MIMI v1.0). *Geoscientific Model Development*, *12*(9), 3835–3862. doi: 10.5194/gmd-12-3835-2019

Hand, J. L., Mahowald, N. M., Chen, Y., Siefert, R. L., Luo, C., Subramaniam, A., & Fung, I. (2004). Estimates of atmospheric-processed soluble iron from observations and a global mineral aerosol model: Biogeochemical implications. *Journal of Geophysical Research D: Atmospheres*, *109*(17), 1–21. doi: 10.1029/2004JD004574

Hand, J. L., Schichtel, B. A., Malm, W. C., & Pitchford, M. L. (2012). Particulate sulfate ion concentration and SO2 emission trends in the United States from the early 1990s through 2010. *Atmospheric Chemistry and Physics*, *12*(21), 10353–10365. doi: 10.5194/acp-12-10353-2012

Harris, R. M., Remenyi, T. A., Williamson, G. J., Bindoff, N. L., & Bowman, D. M. (2016). Climate–vegetation–fire interactions and feedbacks: trivial detail or major barrier to projecting the future of the Earth system? *Wiley Interdisciplinary Reviews: Climate Change*, *7*(6), 910–931. doi: 10.1002/wcc.428

Hoesly, R. M., Smith, S. J., Feng, L., Klimont, Z., Janssens-Maenhout, G., Pitkanen, T., ... Zhang, Q. (2018, jan). Historical (1750–2014) anthropogenic emissions of reactive gases and aerosols from the Community Emissions Data System (CEDS). *Geoscientific Model Development*, *11*(1). doi: 10.5194/gmd-11-369-2018

Hoyle, C. R., Fuchs, C., Järvinen, E., Saathoff, H., Dias, A., El Haddad, I., ... Baltensperger, U. (2016). Aqueous phase oxidation of sulphur dioxide by ozone in cloud droplets. *Atmospheric Chemistry and Physics*, *16*(3), 1693–1712. doi: 10.5194/acp-16-1693-2016

Ito, A. (2015, mar). Atmospheric processing of combustion aerosols as a source of

bioavailable iron. *Environmental Science and Technology Letters*, *2*(3), 70–75. doi: 10.1021/acs.estlett.5b00007

Ito, A., Lin, G., & Penner, J. E. (2018). Radiative forcing by light-absorbing aerosols of pyrogenetic iron oxides. *Scientific Reports*, *8*(1), 1–11. doi: 10.1038/s41598-018-25756-3

Ito, A., Myriokefalitakis, S., Kanakidou, M., Mahowald, N. M., Scanza, R. A., Hamilton, D. S., ... Duce, R. A. (2019). Pyrogenic iron: The missing link to high iron solubility in aerosols. *Science Advances*, *5*(5), 1–11. doi: 10.1126/sciadv.aau7671

Ito, A., & Shi, Z. (2016, jan). Delivery of anthropogenic bioavailable iron from mineral dust and combustion aerosols to the ocean. *Atmospheric Chemistry and Physics*, *16*(1), 85–99. doi: 10.5194/acp-16-85-2016

Ito, A., & Xu, L. (2014, apr). Response of acid mobilization of iron-containing mineral dust to improvement of air quality projected in the future. *Atmospheric Chemistry and Physics*, *14*(7). doi: 10.5194/acp-14-3441-2014

Ito, A., Ye, Y., Baldo, C., & Shi, Z. (2021). Ocean fertilization by pyrogenic aerosol iron. *npj Climate and Atmospheric Science*, *in press*, 1–20. doi: 10.1038/s41612-021-00185-8

Jickells, T., An, Z., Andersen, K., Baker, A., Bergametti, G., Brooks, N., ... Torres, R. (2005, 05). Global iron connections between desert dust, ocean biogeochemistry, and climate. *Science (New York, N.Y.)*, *308*, 67-71. doi: 10.1126/science.1105959

Jickells, T., & Spokes, L. (2001). Atmospheric iron inputs to the oceans. In D. Turner & K. Hunter (Eds.), *The biogeochemistry of iron in seawater* (Vol. SCOR/IUPAC Series, pp. 85–121). Germany: Wiley.

Johnson, K. S. (2001, 03). Iron supply and demand in the upper ocean: Is extraterrestrial dust a significant source of bioavailable iron? *Global Biogeochemical Cycles*, *15*, 61-64. doi: 10.1029/2000GB001295

Johnson, M. S., & Meskhidze, N. (2013). Atmospheric dissolved iron deposition to the global oceans: effects of oxalate-promoted Fe dissolution, photochemical redox cycling, and dust mineralogy. *Geoscientific Model Development*, *6*(4), 1137–1155. doi: 10.5194/gmd-6-1137-2013

Kasoar, M., Hamilton, D., Dalmonech, D., Hantson, S., Lasslop, G., Voulgarakis, A., & Wells, C. (2022). Improved estimates of future fire emissions under cmip6 scenarios and implications for aerosol radiative forcing. , 0–1. (EGU General Assembly 2021) doi: 10.5194/egusphere-egu21-13822

Key, J. M., Paulk, N., & Johansen, A. M. (2008, 1). Photochemistry of iron in simu-

lated crustal aerosols with dimethyl sulfide oxidation products. *Environmental Science and Technology*, *42*, 133-139. doi: 10.1021/es071469y

Koffi, B., Dentener, F., Janssens-Maenhout, G., Guizzardi, D., Crippa, M., Diehl, T., & Galmarini, S. (2016). *Hemispheric Transport Air Pollution (HTAP): Specification of the HTAP2 experiments*. doi: 10.2788/725244

Kok, J. F. (2011, 01). A scaling theory for the size distribution of emitted dust aerosols suggests climate models underestimate the size of the global dust cycle. *Proceedings of the National Academy of Sciences of the United States of America*, *108*, 1016-21. doi: 10.1073/pnas.1014798108

Kok, J. F., Albani, S., Mahowald, N. M., & Ward, D. S. (2014). An improved dust emission model - Part 2: Evaluation in the Community Earth System Model, with implications for the use of dust source functions. *Atmospheric Chemistry and Physics*, *14*(23), 13043–13061. doi: 10.5194/acp-14-13043-2014

Kok, J. F., Ward, D. S., Mahowald, N. M., & Evan, A. T. (2018). Global and regional importance of the direct dust-climate feedback. *Nature Communications*, *9*(1). doi: 10.1038/s41467-017-02620-y

Kundu, S., Kawamura, K., Lee, M., Andreae, T., Hoffer, A., & Andreae, M. (2010, 03). Comparison of amazonian biomass burning and east asian marine aerosols: Bulk organics, diacids and related compounds, water-soluble inorganic ions, stable carbon and nitrogen isotope ratios. *Low Temperature Science*, *68*, 89-100.

Li, F., Koopal, L., & Tan, W. (2018). Roles of different types of oxalate surface complexes in dissolution process of ferrihydrite aggregates. *Scientific Reports*, *8*(1), 1–13. doi: 10.1038/s41598-018-20401-5

Lim, Y. B., Tan, Y., Perri, M. J., Seitzinger, S. P., & Turpin, B. J. (2010, nov). Aqueous chemistry and its role in secondary organic aerosol (SOA) formation. *Atmospheric Chemistry and Physics*, *10*(21). doi: 10.5194/acp-10-10521-2010

Lin, G., Sillman, S., Penner, J. E., & Ito, A. (2014). Global modeling of SOA: The use of different mechanisms for aqueous-phase formation. *Atmospheric Chemistry and Physics*, *14*(11), 5451–5475. doi: 10.5194/acp-14-5451-2014

Lis, H., Shaked, Y., Kranzler, C., Keren, N., & Morel, F. M. (2015). Iron bioavailability to phytoplankton: An empirical approach. *ISME Journal*, *9*, 1003–1013. doi: 10.1038/ismej.2014.199

Liu, J., Horowitz, L. W., Fan, S., Carlton, A. G., & Levy, H. (2012). Global in-cloud production of secondary organic aerosols: Implementation of a detailed chemical mechanism in the GFDL atmospheric model AM3. *Journal of Geophysical Research Atmospheres*, *117*(15), 1–15. doi: 10.1029/2012JD017838

Luo, C., & Gao, Y. (2010). Aeolian iron mobilisation by dust-acid interactions and their implications for soluble iron deposition to the ocean: A test involving potential anthropogenic organic acidic species. *Environmental Chemistry*, *7*(2), 153–161. doi: 10.1071/EN09116

Luo, C., Mahowald, N., Bond, T., Chuang, P. Y., Artaxo, P., Siefert, R., ... Schauer, J. (2008, mar). Combustion iron distribution and deposition. *Global Biogeochemical Cycles*, *22*(1). doi: 10.1029/2007GB002964

Mahowald, N. M. (2007). Anthropocene changes in desert area: Sensitivity to climate model predictions. *Geophysical Research Letters*, *34*(18). doi: 10.1029/2007GL030472

Mahowald, N. M., Baker, A. R., Bergametti, G., Brooks, N., Duce, R. A., Jickells, T. D., ... Tegen, I. (2005). Atmospheric global dust cycle and iron inputs to the ocean. *Global Biogeochemical Cycles*, *19*(4). doi: 10.1029/2004GB002402

Mahowald, N. M., Engelstaedter, S., Luo, C., Sealy, A., Artaxo, P., Benitez-Nelson, C., ... Siefert, R. L. (2009, jan). Atmospheric Iron Deposition: Global Distribution, Variability, and Human Perturbations. *Annual Review of Marine Science*, *1*(1), 245–278. doi: 10.1146/annurev.marine.010908.163727

Mahowald, N. M., Zender, C. S., Luo, C., Savoie, D., Torres, O., & Del Corral, J. (2002). Understanding the 30-year Barbados desert dust record. *Journal of Geophysical Research Atmospheres*, *107*(21), AAC 7–1–AAC 7–16. doi: 10.1029/2002JD002097

Martin, J. H. (1990). Glacial-interglacial co2 change: The iron hypothesis. *Paleoceanography*, *5*(1), 1-13. doi: 10.1029/PA005i001p00001

Martin, J. H., & Fitzwater, S. E. (1988, January). Iron deficiency limits phytoplankton growth in the north-east Pacific subarctic. *Nature*, *331*(6154), 341-343. doi: 10.1038/331341a0

Meskhidze, N., Chameides, W. L., & Nenes, A. (2005). Dust and pollution: A recipe for enhanced ocean fertilization? *Journal of Geophysical Research: Atmospheres*, *110*(D3). doi: 10.1029/2004JD005082

Moxim, W. J., Fan, S. M., & Levy, H. (2011). The meteorological nature of variable soluble iron transport and deposition within the North Atlantic Ocean basin. *Journal of Geophysical Research Atmospheres*, *116*(3), 1–26. doi: 10.1029/2010JD014709

Myriokefalitakis, S., Bergas-Massó, E., Gonçalves-Ageitos, M., Pérez García-Pando, C., Van Noije, T., Le Sager, P., ... Gerasopoulos, E. (2021). Multiphase processes in the EC-Earth Earth System model and their relevance to the atmospheric oxalate, sulfate, and iron cycles. *Geoscientific Model Develop-*

ment(November), 1–71. doi: 10.5194/gmd-2021-357

Myriokefalitakis, S., Daskalakis, N., Gkouvousis, A., Hilboll, A., van Noije, T., Williams, J. E., ... Krol, M. C. (2020). Description and evaluation of a detailed gas-phase chemistry scheme in the tm5-mp global chemistry transport model (r112). *Geoscientific Model Development*, *13*(11), 5507–5548. Retrieved from `https://gmd.copernicus.org/articles/13/5507/2020/` doi: 10.5194/gmd-13-5507-2020

Myriokefalitakis, S., Daskalakis, N., Mihalopoulos, N., Baker, A. R., Nenes, A., & Kanakidou, M. (2015, jul). Changes in dissolved iron deposition to the oceans driven by human activity: a 3-D global modelling study. *Biogeosciences*, *12*(13), 3973–3992. doi: 10.5194/bg-12-3973-2015

Myriokefalitakis, S., Gröger, M., Hieronymus, J., & Döscher, R. (2020). An explicit estimate of the atmospheric nutrient impact on global oceanic productivity. *Ocean Science*, *16*(5), 1183–1205. doi: 10.5194/os-16-1183-2020

Myriokefalitakis, S., Ito, A., Kanakidou, M., Nenes, A., Krol, M. C., Mahowald, N. M., ... Duce, R. A. (2018, nov). *Reviews and syntheses: The GESAMP atmospheric iron deposition model intercomparison study* (Vol. 15) (No. 21). Copernicus GmbH. doi: 10.5194/bg-15-6659-2018

Nenes, A., Krom, M. D., Mihalopoulos, N., Van Cappellen, P., Shi, Z., Bougiatioti, A., ... Herut, B. (2011). Atmospheric acidification of mineral aerosols: a source of bioavailable phosphorus for the oceans. *Atmospheric Chemistry and Physics*, *11*(13), 6265–6272. doi: 10.5194/acp-11-6265-2011

Nickovic, S., Vukovic, A., & Vujadinovic, M. (2013). Atmospheric processing of iron carried by mineral dust. *Atmospheric Chemistry and Physics*, *13*(18), 9169–9181. doi: 10.5194/acp-13-9169-2013

Nickovic, S., Vukovic, A., Vujadinovic, M., Djurdjevic, V., & Pejanovic, G. (2012, 01). Technical note: High-resolution mineralogical database of dust-productive soils for atmospheric dust modeling. *Atmospheric Chemistry and Physics*, *12*, 845-855. doi: 10.5194/acp-12-845-2012

O'Neill, B. C., Tebaldi, C., van Vuuren, D. P., Eyring, V., Friedlingstein, P., Hurtt, G., ... Sanderson, B. M. (2016). The Scenario Model Intercomparison Project (ScenarioMIP) for CMIP6. *Geoscientific Model Development*, *9*(9), 3461–3482. doi: 10.5194/gmd-9-3461-2016

Pausata, F. S., Gaetani, M., Messori, G., Berg, A., Maia de Souza, D., Sage, R. F., & DeMenocal, P. B. (2020). The Greening of the Sahara: Past Changes and Future Implications. *One Earth*, *2*(3), 235–250. doi: 10.1016/j.oneear.2020.03.002

Perlwitz, J. P., Pérez García-Pando, C., & Miller, R. L. (2015a). Predicting the mineral composition of dust aerosols - part 1: Representing key processes. *Atmospheric Chemistry and Physics*, *15*(20), 11593–11627. doi: 10.5194/acp-15-11593-2015

Perlwitz, J. P., Pérez García-Pando, C., & Miller, R. L. (2015b). Predicting the mineral composition of dust aerosols - part 2: Model evaluation and identification of key processes with observations. *Atmospheric Chemistry and Physics*, *15*(20), 11629–11652. doi: 10.5194/acp-15-11629-2015

Pérez García-Pando, C., Miller, R. L., Perlwitz, J. P., Rodríguez, S., & Prospero, J. M. (2016). Predicting the mineral composition of dust aerosols: Insights from elemental composition measured at the izaña observatory. *Geophysical Research Letters*, *43*(19), 10,520-10,529. doi: 10.1002/2016GL069873

Rathod, S. D., Hamilton, D. S., Mahowald, N. M., Klimont, Z., Corbett, J. J., & Bond, T. C. (2020, aug). A mineralogy-based anthropogenic combustion-iron emission inventory. *Journal of Geophysical Research: Atmospheres*, e2019JD032114. doi: 10.1029/2019jd032114

Rizzolo, J. A., Barbosa, C. G. G., Borillo, G. C., Godoi, A. F. L., Souza, R. A. F., Andreoli, R. V., ... Godoi, R. H. M. (2017). Soluble iron nutrients in saharan dust over the central amazon rainforest. *Atmospheric Chemistry and Physics*, *17*(4), 2673–2687. doi: 10.5194/acp-17-2673-2017

Rodríguez, S., Prospero, J. M., López-Darias, J., García-Alvarez, M. I., Zuidema, P., Nava, S., ... Sosa, E. (2021). Tracking the changes of iron solubility and air pollutants traces as African dust transits the Atlantic in the Saharan dust outbreaks. *Atmospheric Environment*, *246*(November 2020). doi: 10.1016/j.atmosenv.2020.118092

Rodriguez-Caballero, E., Stanelle, T., Egerer, S., Cheng, Y., Su, H., Canton, Y., ... Weber, B. (2022). Global cycling and climate effects of aeolian dust controlled by biological soil crusts. *Nature Geoscience*, *15*(6), 458–463. doi: 10.1038/s41561-022-00942-1

Rousset, C., Vancoppenolle, M., Madec, G., Fichefet, T., Flavoni, S., Barthélemy, A., ... Vivier, F. (2015). The Louvain-La-Neuve sea ice model LIM3.6: global and regional capabilities. *Geoscientific Model Development*, *8*(10), 2991–3005. doi: 10.5194/gmd-8-2991-2015

Scanza, R. A., Hamilton, D. S., Perez Garcia-Pando, C., Buck, C., Baker, A., & Mahowald, N. M. (2018, oct). Atmospheric processing of iron in mineral and combustion aerosols: Development of an intermediate-complexity mechanism suitable for Earth system models. *Atmospheric Chemistry and Physics*,

18(19), 14175–14196. doi: 10.5194/acp-18-14175-2018

Schmidl, C., Marr, I. L., Caseiro, A., Kotianová, P., Berner, A., Bauer, H., ... Puxbaum, H. (2008). Chemical characterisation of fine particle emissions from wood stove combustion of common woods growing in mid-European Alpine regions. *Atmospheric Environment*, *42*(1), 126–141. doi: 10.1016/j.atmosenv.2007.09.028

Schroth, A. W., Crusius, J., Sholkovitz, E. R., & Bostick, B. C. (2009). Iron solubility driven by speciation in dust sources to the ocean. *Nature Geoscience*, *2*(5), 337–340. doi: 10.1038/ngeo501

Schulz, M., Prospero, J. M., Baker, A. R., Dentener, F., Ickes, L., Liss, P. S., ... Duce, R. A. (2012). Atmospheric transport and deposition of mineral dust to the ocean: Implications for research needs. *Environmental Science & Technology*, *46*(19), 10390-10404. (PMID: 22994868) doi: 10.1021/es300073u

Shi, Z., Bonneville, S., Krom, M. D., Carslaw, K. S., Jickells, T. D., Baker, A. R., & Benning, L. G. (2011). Iron dissolution kinetics of mineral dust at low ph during simulated atmospheric processing. *Atmospheric Chemistry and Physics*, *11*(3), 995–1007. doi: 10.5194/acp-11-995-2011

Sholkovitz, E. R., Sedwick, P. N., Church, T. M., Baker, A. R., & Powell, C. F. (2012). Fractional solubility of aerosol iron: Synthesis of a global-scale data set. *Geochimica et Cosmochimica Acta*, *89*, 173–189. doi: 10.1016/j.gca.2012.04.022

Smith, S. J., Andres, R., Conception, E., & Lurz, J. (2004). Historical Sulfur Dioxide Emissions 1850-2000 : Methods and Results. *Methods*(January).

Spokes, L. J., Jickells, T. D., & Lim, B. (1994, aug). Solubilisation of aerosol trace metals by cloud processing: A laboratory study. *Geochimica et Cosmochimica Acta*, *58*(15). doi: 10.1016/0016-7037(94)90056-6

Steinfeld, J. I. (1998). Atmospheric Chemistry and Physics: From Air Pollution to Climate Change. *Environment: Science and Policy for Sustainable Development*, *40*(7), 26. doi: 10.1080/00139157.1999.10544295

Stoll, H. (2020). 30 years of the iron hypothesis of ice ages. *Nature: International Weekly Journal of Science*, *578*(7795), 370–371. doi: 10.1038/d41586-020-00393-x

Tegen, I., Harrison, S. P., Kohfeld, K., Prentice, I. C., Coe, M., & Heimann, M. (2002). Impact of vegetation and preferential source areas on global dust aerosol: Results from a model study. *Journal of Geophysical Research: Atmospheres*, *107*(D21), AAC 14-1-AAC 14-27. doi: 10.1029/2001JD000963

Tsai, I. C., Chen, J. P., Lin, P. Y., Wang, W. C., & Isaksen, I. S. (2010). Sulfur

cycle and sulfate radiative forcing simulated from a coupled global climate-chemistry model. *Atmospheric Chemistry and Physics*, *10*(8), 3693–3709. doi: 10.5194/acp-10-3693-2010

Van Noije, T., Bergman, T., Le Sager, P., O'Donnell, D., Makkonen, R., Gonçalves-Ageitos, M., ... Yang, S. (2021). EC-Earth3-AerChem: A global climate model with interactive aerosols and atmospheric chemistry participating in CMIP6. *Geoscientific Model Development*, *14*(9), 5637–5668. doi: 10.5194/gmd-14-5637-2021

Vancoppenolle, M., Fichefet, T., Goosse, H., Bouillon, S., Madec, G., & Maqueda, M. A. M. (2009). Simulating the mass balance and salinity of Arctic and Antarctic sea ice. 1. Model description and validation. *Ocean Modelling*, *27*(1), 33–53. doi: 10.1016/j.ocemod.2008.10.005

van Marle, M. J. E., Kloster, S., Magi, B. I., Marlon, J. R., Daniau, A.-L., Field, R. D., ... van der Werf, G. R. (2017). Historic global biomass burning emissions for CMIP6 (BB4CMIP) based on merging satellite observations with proxies and fire models (1750–2015). *Geoscientific Model Development*, *10*(9), 3329–3357. doi: 10.5194/gmd-10-3329-2017

Vignati, E., Wilson, J., & Stier, P. (2004). M7: An efficient size-resolved aerosol microphysics module for large-scale aerosol transport models. *Journal of Geophysical Research: Atmospheres*, *109*(D22). doi: 10.1029/2003JD004485

Wagner, R., Jähn, M., & Schepanski, K. (2018). Wildfires as a source of airborne mineral dust - Revisiting a conceptual model using large-eddy simulation (LES). *Atmospheric Chemistry and Physics*, *18*(16), 11863–11884. doi: 10.5194/acp-18-11863-2018

Wang, R., Balkanski, Y., Boucher, O., Bopp, L., Chappell, A., Ciais, P., ... Tao, S. (2015, jun). Sources, transport and deposition of iron in the global atmosphere. *Atmospheric Chemistry and Physics*, *15*(11), 6247–6270. doi: 10.5194/acp-15-6247-2015

Ward, D. S., Kloster, S., Mahowald, N. M., Rogers, B. M., Randerson, J. T., & Hess, P. G. (2012). The changing radiative forcing of fires: Global model estimates for past, present and future. *Atmospheric Chemistry and Physics*, *12*(22), 10857–10886. doi: 10.5194/acp-12-10857-2012

Warneck, P. (2003). In-cloud chemistry opens pathway to the formation of oxalic acid in the marine atmosphere. *Atmospheric Environment*, *37*(17), 2423–2427. doi: 10.1016/S1352-2310(03)00136-5

Wu, C., Lin, Z., & Liu, X. (2020). Global dust cycle and uncertainty in CMIP5 models. *Atmospheric Chemistry and Physics Discussions*, *5*, 1–52.

Yamasoe, M. A., Artaxo, P., Miguel, A. H., & Allen, A. G. (2000). Chemical composition of aerosol particles from direct emissions of vegetation fires in the Amazon Basin: water-soluble species and trace elements. *Atmospheric Environment*, *34*(10), 1641–1653. doi: 10.1016/S1352-2310(99)00329-5

Yoon, T. H., Johnson, S. B., Musgrave, C. B., & Brown, G. E. (2004). Adsorption of organic matter at mineral/water interfaces: I. ATR-FTIR spectroscopic and quantum chemical study of oxalate adsorbed at boehmite/water and corundum/water interfaces. *Geochimica et Cosmochimica Acta*, *68*(22), 4505–4518. doi: 10.1016/j.gca.2004.04.025

Yoshioka, M., Mahowald, N. M., Conley, A. J., Collins, W. D., Fillmore, D. W., Zender, C. S., & Coleman, D. B. (2007). Impact of desert dust radiative forcing on sahel precipitation: Relative importance of dust compared to sea surface temperature variations, vegetation changes, and greenhouse gas warming. *Journal of Climate*, *20*(8), 1445–1467. doi: 10.1175/JCLI4056.1

Yu, Y., & Ginoux, P. (2022). Enhanced dust emission following large wildfires due to vegetation disturbance. *Nature Geoscience*(October). doi: 10.1038/s41561-022-01046-6

Yu, Y., Mao, J., Wullschleger, S. D., Chen, A., Shi, X., Wang, Y., ... Pierce, E. (2022). Machine learning–based observation-constrained projections reveal elevated global socioeconomic risks from wildfire. *Nature Communications*, *13*(1), 1–11. doi: 10.1038/s41467-022-28853-0

Zhuang, G., Yi, Z., Duce, R., & Brown, P. (1992a, 02). Link between iron and sulfur cycles suggested by fe(ii) in remote marine aerosol. In *Nature* (Vol. 355, p. 537-539).

Zhuang, G., Yi, Z., Duce, R. A., & Brown, P. R. (1992b, feb). Link between iron and sulphur cycles suggested by detection of Fe(n) in remote marine aerosols. *Nature*, *355*(6360). doi: 10.1038/355537a0